Article

A Finite Volume-based Unified Transient Deterministic Framework for Lubrication Modelling

Filimonas Kaliafetis [1,*], Daniele Dini [1], James P. Ewen [1,2] and Suhaib Ardah [1]

[1] Department of Mechanical Engineering, Imperial College London, Exhibition Road, South Kensington, London, SW7 2AZ, United Kingdom;
[2] Department of Mechanical Engineering, University of Bath, Claverton Down, Bath, BA2 7AY, United Kingdom
* Correspondence: f.kaliafetis23@imperial.ac.uk;

Abstract

A transient deterministic unified lubrication model is developed for the analysis of rough, starved, and coated contacts within a single, fully coupled numerical framework capable of resolving boundary, mixed, and full-film lubrication regimes. The model is formulated with the finite volume method on a curvilinear grid and extends conventional full-film formulations through the introduction of a semi-system methodology, enabling robust treatment of complex multi-regime conditions. A key distinguishing feature of the framework is the direct resolution of thermal effects within both the lubricant and solid domains through solution of the energy equation. Unlike many existing mixed lubrication models that rely on analytical temperature approximations, the present approach captures transient, asperity-scale temperature evolution explicitly, allowing accurate representation of local thermo-mechanical interactions. Two case studies are presented to demonstrate the capabilities of the model. The first examines transient starvation in rough contacts with isotropic sinusoidal topographies of varying wavelength, revealing a strong dependence of lubricant entrainment, asperity interaction, and localised heating on surface morphology. Certain wavelengths promote hydrodynamic film recovery, whereas others lead to pronounced asperity contact and elevated thermal gradients. The second study investigates the role of coating thermal properties under transient starved conditions, demonstrating a strong coupling between heat transport, viscosity variations, and frictional response. Overall, the proposed framework provides a robust and physically consistent platform for the simulation of transient lubrication phenomena under realistic operating conditions, enabling detailed insight into roughness, starvation, and thermal effects across regimes using a fully coupled approach.

1. Introduction

Elastohydrodynamic lubrication (EHL) plays a central role in the performance and durability of heavily loaded machine elements such as gears, bearings, and other rolling-sliding contacts [1]. Over the past few decades, significant progress has been made in the development of numerical models capable of predicting pressure, film thickness and friction under a wide range of operating conditions. In particular, the introduction of fully coupled thermal frameworks and advanced numerical methods, such as finite element and finite volume approaches, has enabled increasingly accurate simulations of EHL contacts, including the effects of non-Newtonian rheology and heat generation within the lubricant and solid bodies [2].

Early numerical developments primarily focused on smooth surfaces and steady-state, fully flooded conditions [3]. However, it is now well established that real engineering contacts operate under far more complex conditions, where surface roughness, transient effects, thermal phenomena and lubricant starvation can all play a significant role. As a result, a large body of research has emerged addressing these individual effects [1,2].

In particular, lubricant starvation is now recognised as a common operating condition in important components, such as high-speed rolling-element bearings [4]. Starvation often arises unintentionally

due to insufficient oil supply or redistribution of lubricant within the system. Experimental studies have shown that even small variations in available lubricant volume can significantly alter frictional behaviour and transition the contact toward mixed lubrication regimes, strongly affecting component life and efficiency [5]. Starvation effects are also closely linked to operating conditions such as entrainment speed, surface finish, and contact geometry, and can lead to markedly different tribological responses depending on the initial lubricant distribution and surface structure [6].

Transient starvation has been studied in smooth EHL contacts where time-dependent inlet boundary conditions and lubricant supply limitations are considered. Recent contributions have demonstrated the importance of starvation dynamics on film thickness and friction evolution [7]. However, these models are generally restricted to smooth surfaces and full-film lubrication regimes, without considering deterministic surface roughness or asperity interactions.

Other models have extended the analysis to rough surfaces [8]. For example, studies considering roughness effects under starved conditions have shown that cavitation is more pronounced in textured or dented surfaces under starved lubrication regimes [9]. Additional investigations into rough surface interactions under starvation have also demonstrated that surface finish plays a critical role in determining frictional behaviour and lubrication efficiency, with different roughness structures leading to distinct starvation responses [10]. However, these formulations typically neglect thermal effects and do not resolve asperity-level contact interactions.

The importance of starvation has also been highlighted in more complex geometries and operating conditions. For example, in elliptical and circular EHL contacts, it has been shown that the lubricant inlet layer thickness governs a transition towards a quasi-fully flooded regime, where further increases in lubricant supply have diminishing influence on film formation [11]. In finite line contacts such as gears and bearings, starvation has been shown to strongly influence friction, film thickness and fatigue life, with pronounced sensitivity to operating speed and slide-to-roll ratio [12]. Similarly, other studies of rolling bearings demonstrate that starvation not only affects film thickness, but also alters contact forces and dynamic stability of the system [13]. These findings highlight that starvation is inherently coupled with system dynamics and cannot be treated as a purely inlet-boundary phenomenon.

Further developments have introduced thermal coupling and asperity contacts within starved EHL systems. In particular, models incorporating rough surfaces, thermal effects and asperity interactions have demonstrated the strong coupling between temperature rise and film reduction in starved conditions [14]. These studies show that the presence of roughness significantly intensifies local heating at asperity contacts, which in turn accelerates film thinning and promotes inter-asperity cavitation, particularly under reduced inlet supply conditions. Nevertheless, such approaches commonly rely on simplified thermal treatments, where the solid-body temperature evolution is estimated using analytical flash temperature formulations based on Carslaw-Jaeger theory [15] rather than solving the full energy equation within the solids. As a result, the spatial and transient evolution of temperature within the solid bodies cannot be fully resolved, limiting the ability to capture subsurface thermal gradients and their influence on local contact conditions.

In parallel, deterministic modelling of surface roughness has become an important research area. Several studies have investigated the transient passage of surface features through EHL contacts, showing that asperities can induce strong local variations in pressure, film thickness and temperature. These models have been extended to mixed lubrication conditions, where load sharing between asperities and the lubricant is considered [6,16]. However, thermal effects are again commonly simplified using analytical flash temperature models (e.g. Archard [17] or Carslaw-Jaeger-type [15] approximations) rather than being resolved through solution of the full energy equation within the solids. Such empirical approximations inherently neglect the transient evolution of temperature fields within the contacting bodies. Consequently, heat penetration, diffusion and accumulation within the solids remain poorly resolved in most existing thermo-EHL frameworks.

Surface coatings have also received considerable attention, due to their ability to modify both mechanical compliance and thermal behaviour of EHL contacts [18]. Previous studies have demonstrated

that coating thickness, elastic modulus, and thermal inertia significantly influence pressure distribution, film thickness, and frictional response. For instance, coated EHL contacts have been analysed under both mechanical and thermal variations, showing clear sensitivity to material properties [19]. However, most existing coating models are limited to steady-state conditions and transient effects have not been widely addressed within a fully coupled thermal framework.

Although these phenomena, namely transient starvation, deterministic roughness, thermal asperity interactions and coatings, have been studied individually, they are rarely considered within a single unified modelling framework. In particular, existing approaches tend to separate full-film, mixed and boundary lubrication regimes, or simplify thermal effects at asperity level, limiting their applicability to realistic operating conditions.

Furthermore, the studies mentioned above predominantly employ either the finite difference method (FDM) or the finite element method (FEM) to discretise the governing equations. FDM-based approaches have been widely adopted in EHL due to their relatively straightforward implementation and computational efficiency, particularly for Reynolds-equation-based formulations and unified mixed lubrication models [6,16,20]. FEM formulations, on the other hand, have proven particularly effective for strongly coupled thermo-mechanical problems involving complex geometries, non-linear material behaviour and coated contacts [19]. Nevertheless, comparatively few studies have explored the use of the finite volume method (FVM) for TEHL applications, despite its inherent conservation properties and suitability for coupled transport problems involving mass, momentum and energy conservation. Existing FVM-based EHL studies [21–23] are generally limited to smooth full-film conditions and rarely incorporate deterministic roughness, asperity interactions, starvation or unified mixed lubrication formulations. A recent study studied surface textures in ball-on-disc tribometers under unsteady operating conditions using a FVM framework [24]. However, that was done at isothermal conditions and without considering starvation. An even more recent study [25] combined the geometric flexibility of the FEM with the conservation properties of the FVM into an Element-based Finite Volume Method (EbFVM) to study multiphysics transport problems in textured journal bearing systems. Once again, though, asperity interactions, transient behaviours, starvation and coatings were not taken into consideration.

As a result, there remains a need for a comprehensive numerical model capable of simultaneously capturing transient behaviour, deterministic surface roughness, asperity-scale thermal effects, lubricant starvation and coating behaviour within a unified formulation.

In this work, a transient deterministic unified lubrication model is developed within a FVM framework on a curvilinear grid. The formulation extends previous full-film thermal EHL solvers [26,27] to a unified treatment of boundary, mixed and full-film lubrication regimes through the use of a semi-system approach [20], enabling robust and consistent solution behaviour across contact conditions. In contrast to most existing unified mixed lubrication models, the present approach employs a fully conservative FVM framework capable of consistently resolving coupled flow and thermal transport within the lubricant, coatings and solid domains.

Building on this framework, several key advancements are introduced. First, asperity-scale thermal effects are directly resolved through the solution of the energy equation in both the lubricant and solid domains, allowing the transient temperature distribution within the contacting bodies to be captured without reliance on analytical approximations such as Carslaw-Jaeger theory. Second, the model takes into consideration the transient behaviour of systems with surface coatings, enabling the analysis of layered materials under realistic operating conditions. Finally, transient lubricant starvation is considered in combination with deterministic surface roughness and asperity contacts, a capability that, to the authors' knowledge, has not previously been reported.

2. Methodology

2.1. Coupled Thermo-Hydrodynamic Lubrication Framework

The unified multiphysics lubrication framework developed in this study builds upon the steady-state thermal lubrication formulations previously proposed in [26,27] for both line and point contact configurations. These earlier models incorporated mass-conserving cavitation algorithms, and were extensively validated against experimental measurements and high-fidelity CFD simulations, demonstrating excellent predictive capability in the evaluation of pressure, temperature, film thickness, and friction under steady-state conditions for smooth lubricated interfaces. In addition, the point contact implementation has recently been used to generate high-fidelity thermo-lubrication datasets for artificial neural network-based acceleration of lubrication simulations [28], further demonstrating the robustness, computational consistency, and predictive value of the underlying framework. The present contribution extends these formulations to transient rough surface lubrication problems involving deformable coated interfaces. In particular, the framework enables the fully coupled interaction between deterministic surface topography, hydrodynamic flow, thermal transport, cavitation, and asperity contact to be resolved within a unified computational setting. This provides a rigorous and consistent description of lubrication behaviour under highly transient operating conditions, where local asperity interactions, lubricant starvation, and coating-induced thermal effects may strongly influence the interfacial response. This is achieved through a semi-system formulation [20,29], whereby the governing equations remain valid throughout the entire computational domain, including regions of vanishing film thickness corresponding to asperity contact. Consequently, the transition between full-film lubrication and asperity contact is captured implicitly, without the need for separate contact models or artificial switching criteria between lubrication regimes. This unified treatment enhances numerical robustness and enables a consistent description of lubrication behaviour across hydrodynamic, mixed, and boundary lubrication regimes.

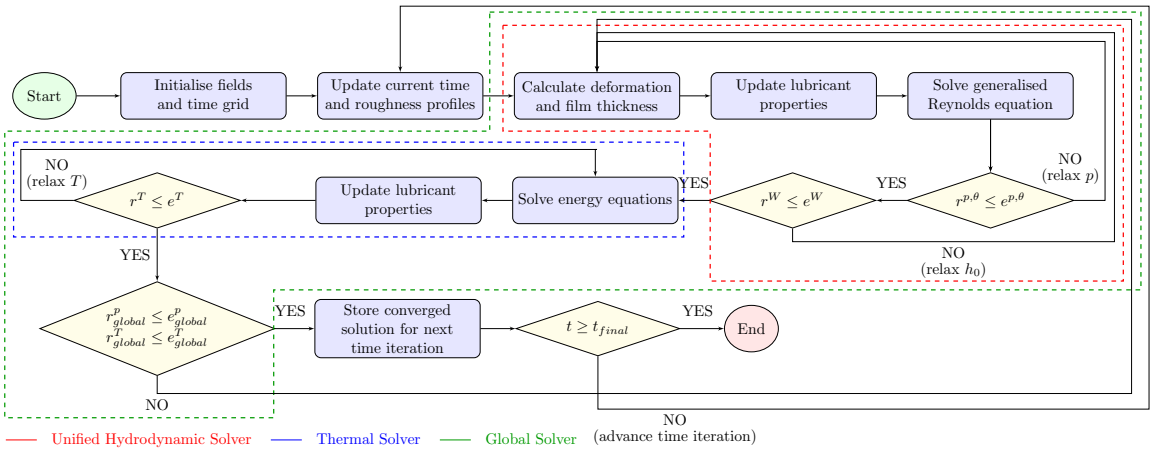

Figure 1. Numerical solution strategy for the fully coupled transient lubrication framework.

As shown in Figure 1, the solution procedure is based on a fully coupled time-marching algorithm in which the governing equations are solved sequentially within each discrete time step while preserving the strong coupling between hydrodynamic, thermal, and interfacial phenomena. At the beginning of the simulation ($t = 0$), the temporal discretisation is defined and the primary field variables, including pressure, temperature, film thickness, and lubricant film fraction, are initialised. During each subsequent time increment, the rough surface topography is advanced through the computational domain either by spatial translation or through a progressive evolution of the roughness amplitude, thereby enabling transient rough surface interactions to be captured explicitly. Within each time step, the coupled lubrication problem is solved iteratively through a global nonlinear solution loop. The isothermal lubrication problem is solved first in order to obtain converged pressure, lubricant film fraction, and film thickness distributions satisfying the externally applied load. Convergence of the

hydrodynamic solution is achieved when the combined pressure-film fraction residual, $r^{p,\theta}$, falls below the prescribed convergence tolerance, $e^{p,\theta}$. Simultaneously, load equilibrium is enforced through the load residual r^W, which must satisfy the convergence criterion e^W.

Once hydrodynamic convergence has been achieved, the thermal problem is solved using the converged pressure and film thickness fields. The energy equations governing the lubricant film, coating layers, and solid domains are solved iteratively until the temperature residual r^T becomes smaller than the thermal convergence tolerance e^T. Following thermal convergence, the global pressure and temperature residuals, r^p_{global} and r^T_{global}, are evaluated to assess convergence of the fully coupled multiphysics system. Global convergence for a given time step is achieved once both residuals satisfy their corresponding tolerances, e^p_{global} and e^T_{global}. The converged solution is subsequently stored and used to initialise the following time step. This introduces the required temporal continuity and history dependence necessary for resolving transient thermo-hydrodynamic and asperity-scale phenomena. The solution procedure is then repeated until the final simulation time is reached.

The residual measures employed throughout the solution procedure are defined as follows:

$$r^{p,\theta} = \frac{\sum_{i=1}^{N_x}\sum_{j=1}^{N_y}\left|p^n_{i,j} - p^{n-1}_{i,j}\right|}{\sum_{i=1}^{N_x}\sum_{j=1}^{N_y}\left|p^n_{i,j}\right|} + \frac{\sum_{i=1}^{N_x}\sum_{j=1}^{N_y}\left|\theta^n_{i,j} - \theta^{n-1}_{i,j}\right|}{\sum_{i=1}^{N_x}\sum_{j=1}^{N_y}\left|\theta^n_{i,j}\right|}, \tag{1a}$$

$$r^W = \frac{\left|W - \iint_\Omega p(x,y)\,dx\,dy\right|}{W}, \tag{1b}$$

$$r^T = \frac{\sum_{i=1}^{N_x}\sum_{j=1}^{N_y}\sum_{k=1}^{N_z}\left|T^n_{i,j,k} - T^{n-1}_{i,j,k}\right|}{\sum_{i=1}^{N_x}\sum_{j=1}^{N_y}\sum_{k=1}^{N_z}\left|T^n_{i,j,k}\right|}, \tag{1c}$$

$$r^p_{\text{global}} = \frac{\sum_{i=1}^{N_x}\sum_{j=1}^{N_y}\left|p^g_{i,j} - p^{g-1}_{i,j}\right|}{\sum_{i=1}^{N_x}\sum_{j=1}^{N_y}\left|p^g_{i,j}\right|}, \tag{1d}$$

$$r^T_{\text{global}} = \frac{\sum_{i=1}^{N_x}\sum_{j=1}^{N_y}\sum_{k=1}^{N_z}\left|T^g_{i,j,k} - T^{g-1}_{i,j,k}\right|}{\sum_{i=1}^{N_x}\sum_{j=1}^{N_y}\sum_{k=1}^{N_z}\left|T^g_{i,j,k}\right|}. \tag{1e}$$

Here, i, j, and k denote the nodal indices in the x-, y-, and z-directions, respectively, while N_x, N_y, and N_z correspond to the number of discretisation points along each coordinate direction. The superscript n denotes the current iteration within the hydrodynamic or thermal sub-solvers, whereas g denotes the iteration level associated with the global coupled solution procedure.

2.1.1. Hydrodynamic Flow and Mass Conservation

The hydrodynamic behaviour of the confined lubrication film is described using the generalised Reynolds equation that accounts for spatiotemporal variations in film thickness $h(x,y,t)$, lubricant viscosity $\eta(x,y,t)$, and density $\rho(x,y,t)$, together with the kinematics of the bounding surfaces [30].

The latter are defined by the velocity fields $v_1 = \begin{bmatrix} u_1 & v_1 \end{bmatrix}^T$ and $v_2 = \begin{bmatrix} u_2 & v_2 \end{bmatrix}^T$ in the x- and y-directions pertaining to the lower and upper surfaces, respectively. To ensure a physically consistent treatment of lubricant rupture and reformation, a mass-conserving p–θ formulation based on the Elrod-Adams cavitation algorithm is employed [31–33]. This approach enforces the Jakobsson-Floberg-Olsson (JFO) complementary conditions [34–36], enabling a robust description of pressurised and cavitated regions within the lubricated domain. Accordingly, the coupled pressure-film fraction (p–θ) form of the generalised Reynolds equation (GRE) is expressed in conservative form as follows:

$$\underbrace{\frac{\partial}{\partial x}\left(\varepsilon\frac{\partial p}{\partial x}\right)+\frac{\partial}{\partial y}\left(\varepsilon\frac{\partial p}{\partial y}\right)}_{\text{Pressure flow terms}}=\underbrace{\frac{\partial(\theta\rho_x^*)}{\partial x}+\frac{\partial(\theta\rho_y^*)}{\partial y}}_{\text{Entraining flow terms}}+\underbrace{\frac{\partial(\theta\rho_e)}{\partial t}}_{\text{Transient term}}. \tag{2}$$

The effective transport coefficients in Equation 2 that take into account the variations of viscosity and density across the film thickness are defined as follows:

$$\varepsilon=\frac{\eta_e}{\eta_e'}\rho'-\rho'', \qquad \rho_x^*=\rho_e u_1+\eta_e u_s\rho',$$
$$\rho_y^*=\rho_e v_1+\eta_e v_s\rho', \qquad \rho_e=\int_{z_1}^{z_2}\rho\,dz,$$
$$\frac{1}{\eta_e}=\int_{z_1}^{z_2}\frac{dz}{\eta}, \qquad \rho'=\int_{z_1}^{z_2}\rho\left(\int_{z_1}^{z}\frac{dz'}{\eta}\right)dz,$$
$$\frac{1}{\eta_e'}=\int_{z_1}^{z_2}\frac{z\,dz}{\eta}, \qquad \rho''=\int_{z_1}^{z_2}\rho\left(\int_{z_1}^{z}\frac{z'\,dz'}{\eta}\right)dz.$$

Additionally, the coexistence of pressurised and cavitated regions is governed by a set of complementarity conditions which enforces the mutually exclusive states as follows:

$$(p-p_{cav})(1-\theta)=0\rightarrow\begin{cases} p>p_{cav} & \rightarrow \quad \theta=1 & \text{(fully flooded)},\\ p=p_{cav} & \rightarrow \quad 0\leq\theta<1 & \text{(cavitated region)}, \end{cases} \tag{3}$$

where p_{cav} denotes the cavitation pressure, while $\theta = \rho/\rho_c$ represents the fluid fraction, with ρ_c corresponding to the density of the saturated lubricant at cavitation conditions.

This formulation naturally extends to the modelling of inlet starvation by prescribing the film fraction at the inlet as a function of the available lubricant supply. Specifically, the film fraction is defined through the ratio of the supplied lubricant thickness h_{oil} to the local geometric film thickness h, such that:

$$\theta=\frac{h_{\text{oil}}}{h}. \tag{4}$$

Here, h_{oil} represents the thickness of lubricant available at the inlet, thereby limiting the local film formation when $\theta < 1$. This approach provides a physically consistent and mass-conserving representation of starvation within the p–θ framework, without the need for additional boundary conditions or empirical corrections.

The finite volume discretisation of the GRE as well as the energy equations for the fluid and solid bodies can be found in Appendix A.

2.1.2. Deterministic Representation of Surface Roughness

Surface roughness is incorporated using a fully deterministic framework based on the approach of Hu and Zhu [37], in which the roughness field is explicitly resolved within the governing equations, rather than treated through stochastic or homogenised approximations. Within this formulation, the generalised Reynolds equation is applied consistently across the entire computational domain to

capture both hydrodynamic pressure generation in regions of finite film thickness ($h > 0$) and contact pressure in regions where the lubricant film collapses ($h \to 0$). The transition between these regimes is handled implicitly through a local modification of the governing equation, thereby avoiding the need for separate contact models or domain decomposition.

In regions where a continuous lubricant film is present, the full form of the generalised Reynolds equation (Equation 2) is retained. However, when the local film thickness approaches zero, the pressure-driven (Poiseuille) flow contribution becomes negligible. In such cases, the governing equation reduces to the following form:

$$\frac{\partial(\theta\rho_x^*)}{\partial x} + \frac{\partial(\theta\rho_y^*)}{\partial y} + \frac{\partial(\theta\rho_e)}{\partial t} = 0, \tag{5}$$

which represents a balance between entrainment and transient mass transport in the absence of pressure-driven flow.

On the other hand, in asperity contact regions where the film thickness is locally constant (*i.e.* negligible spatial gradients), the transient contribution becomes insignificant, leading to the following simplified form:

$$\frac{\partial(\theta\rho_x^*)}{\partial x} + \frac{\partial(\theta\rho_y^*)}{\partial y} = 0, \tag{6}$$

which describes purely advective transport along the lubricated interface.

Therefore, the appropriate form of the governing equation is selected locally based on the relative magnitude of the film thickness and its spatial gradient. Specifically, the following criteria are employed:

$$\text{Hydrodynamic governing equation} \quad \to \quad \begin{cases} \text{Equation 2}, & \text{if } \dfrac{h}{a} > \varepsilon_h, \\ \text{Equation 5}, & \text{if } \dfrac{h}{a} < \varepsilon_h, \text{ and } \dfrac{\partial h}{\partial x} > \varepsilon_s, \\ \text{Equation 6}, & \text{if } \dfrac{h}{a} < \varepsilon_h, \text{ and } \dfrac{\partial h}{\partial x} < \varepsilon_s, \end{cases}$$

where a denotes the characteristic length scale of the contact (taken here as the Hertzian contact radius), while $\varepsilon_h = 10^{-6}$ and $\varepsilon_s = 10^{-5}$ are the prescribed numerical tolerances used to distinguish between full-film, transition, and asperity contact regimes. These thresholds are chosen to ensure numerical robustness while maintaining a physically consistent identification of regions with diminishing lubricant film thickness and negligible surface gradients.

These conditions are evaluated locally during every time step, enabling a fully transient and spatially resolved treatment of rough surface interactions. This local and dynamic adaptation of the governing equations ensures that hydrodynamic and contact responses are captured consistently and simultaneously within a single computational framework, without the need for pre-defined regime separation. The simulation is initialised using a smooth surface solution, which provides a numerically stable baseline for the subsequent deterministic evolution of the roughness field. As the simulation progresses, the rough surface is advected through the computational domain, allowing the time-dependent interaction between surface topography, lubricant flow, and interfacial contact to be resolved explicitly. This approach is adopted in order to capture of transient phenomena arising from asperity-scale interactions, including localised film collapse, pressure redistribution, and the intermittent formation of contact regions. As such, the framework provides a physically consistent description of lubrication behaviour in rough interfaces, beyond the limitations of homogenised or stochastic roughness models.

2.1.3. Film Thickness and Interface Deformation

The local geometry of the lubricant film is described by a coupled representation that accounts for macroscopic surface curvature, elastic deformation, and time-dependent surface roughness. For a

point contact configuration, the film thickness distribution is expressed in Cartesian coordinates as follows:

$$h(x,y,t) = h_0 + \frac{x^2}{2R_x} + \frac{y^2}{2R_y} + \delta(x,y) + s_1(x,y,t) + s_2(x,y,t), \tag{7}$$

where h_0 denotes the rigid body separation, and R_x and R_y are the equivalent radii of curvature along the x- and y-directions, respectively (with $R_x = R_y = R$ for circular contacts). The terms s_1 and s_2 represent the time-dependent surface roughness profiles of the two contacting solids, which are explicitly resolved within the computational domain.

The normal elastic deformation $\delta(x,y)$ arises from the hydrodynamic pressure distribution and is evaluated using the classical Boussinesq solution for an elastic half-space problem. This is expressed as the convolution integral which reads as follows:

$$\delta(x,y) = \frac{2}{\pi E'} \iint_{\Omega} \frac{p(\xi,\varsigma)}{\sqrt{(x-\xi)^2 + (y-\varsigma)^2}}\, d\xi\, d\varsigma, \tag{8}$$

where $p(\xi,\varsigma)$ denotes the pressure distribution over the contact domain Ω, and E' is the reduced elastic modulus of the contacting pair, defined as:

$$\frac{2}{E'} = \frac{1-\nu_1^2}{E_1} + \frac{1-\nu_2^2}{E_2},$$

with $E_{1,2}$ and $\nu_{1,2}$ representing the Young's moduli and Poisson's ratios of the respective solids. For computational efficiency, the convolution in Equation 8 is evaluated using the discrete convolution fast Fourier transform (DC-FFT) method, which provides an efficient route for computing elastic deformation in contact problems. By combining influence coefficients with zero padding and wrap-around ordering, the DC-FFT method converts the linear convolution into a cyclic convolution suitable for FFT evaluation, while avoiding the periodic errors associated with conventional FFT-based approaches [38,39].

2.1.4. Surface Coating Deformation

The mechanical response of coated interfaces under loading is evaluated using the analytical multilayer elastic solution proposed by Yu et al. [40]. In this approach, the coated solid is represented as an elastic half-space covered by L coating layers, where each layer is indexed by $j = \{1, \ldots, L\}$ and the substrate is denoted by $j = L+1$. Each layer is assigned an individual thickness h_j, Young's modulus E_j, and Poisson's ratio ν_j, and is assumed to behave as a linear elastic, homogeneous, and isotropic material. This formulation enables coating-induced compliance effects to be incorporated directly into the evolving lubricant film geometry through the pressure-deformation coupling.

The displacement field within each layer is described using a frequency-domain solution based on Papkovich-Neuber elastic potentials. Under normal loading, the transformed normal discplacement in layer j is expressed as follows:

$$\begin{aligned}\tilde{\tilde{u}}_3^{(j)} =& \frac{1}{2G_j}\Big\{ -\alpha[A^{(j)}e^{-\alpha z_j} - \overline{A}^{(j)}e^{\alpha z_j}] + imz_j[B^{(j)}e^{-\alpha z_j} + \overline{B}^{(j)}e^{\alpha z_j}] \\ & - im\alpha^{-1}[B^{(j)}e^{-\alpha z_j} - \overline{B}^{(j)}e^{\alpha z_j}] - (3-4\nu_j)[C^{(j)}e^{-\alpha z_j} + \overline{C}^{(j)}e^{\alpha z_j}] \\ & - \alpha z_j[C^{(j)}e^{-\alpha z_j} - \overline{C}^{(j)}e^{\alpha z_j}] - i\alpha[B_{,m}^{(j)}e^{-\alpha z_j} - \overline{B}_{,m}^{(j)}e^{\alpha z_j}]\Big\},\end{aligned} \tag{9}$$

where '$\approx$' indicates a double Fourier transform operation, i is the imaginary unit, and $\alpha = \sqrt{m^2+n^2}$, where m and n are transformed frequency variables in the x- and y-directions respectively. The coordinate z_j denotes the out-of-plane coordinate with layer j, while $G_j = \frac{E_j}{2(1+\nu_j)}$ is the shear modulus

of each layer. The coefficients $A^{(j)}$, $\overline{A}^{(j)}$, $B^{(j)}$, $\overline{B}^{(j)}$, $C^{(j)}$, $\overline{C}^{(j)}$, $B_{,m}^{(j)}$ and $\overline{B}_{,m}^{(j)}$ are obtained from the multilayer elastic solution described by Yu et al. [40] in Appendix C.

In the present study, the quantity of interest is the normal surface displacement induced by the hydrodynamic pressure filed, corresponding to the deformation term $\delta(x,y)$ in the film thickness formulation. The frequency response function of the normal surface displacement is therefore determined by evaluating the displacement expression at the coated surface, $z_j = 0$, for the top layer, $j = 1$, giving the following expression:

$$\begin{aligned}\tilde{\tilde{G}}^{u_3}(m,n,0) = -\frac{1}{2G_1}\Big\{&\alpha[A^{(1)} - \overline{A}^{(1)}] + im\alpha^{-1}[B^{(1)} - \overline{B}^{(1)}] \\ &+ (3-4\nu_1)[C^{(1)} + \overline{C}^{(1)}] + i\alpha[B_{,m}^{(1)} - \overline{B}_{,m}^{(1)}]\Big\}.\end{aligned} \tag{10}$$

The resulting frequency response function is then used to construct the continuous influence coefficient for normal surface displacement ($\tilde{\tilde{D}}^{u_3}$), as follows [41]:

$$\tilde{\tilde{D}}^{u_3}(m,n) = \tilde{\tilde{G}}^{u_3}(m,n) \cdot \tilde{\tilde{Y}}(m,n), \tag{11}$$

where $\tilde{\tilde{Y}}$ is the shape function, defined as $\tilde{\tilde{Y}}(m,n) = \frac{4\sin(m\Delta_x)\sin(n\Delta_y)}{mn}$. The Fourier-transformed frequency variables are evaluated as follows:

$$\begin{aligned} m &= \frac{2\pi}{M_e\Delta_x}i - r_x\frac{2\pi}{\Delta_x}, \qquad i = \{0,...,\frac{M_e}{2}-1\}, \\ n &= \frac{2\pi}{N_e\Delta_y}j - r_y\frac{2\pi}{\Delta_y}, \qquad j = \{0,...,\frac{N_e}{2}-1\}. \end{aligned} \tag{12}$$

Here, $M_e = 2^{\gamma_{mesh}}N_x$ and $N_e = 2^{\gamma_{mesh}}N_y$, where N_x and N_y are the number of grid points in the x- and y-directions, respectively, γ_{mesh} is the mesh refinement coefficient, and Δ_x and Δ_y are the spatial grid spacings in the x- and y-directions, respectively.

The continuous influence coefficients are subsequently converted into discrete influence coefficients as follows:

$$\hat{\tilde{D}}^{u_3}(m,n) = \frac{1}{\Delta_x\Delta_y}\sum_{r_x=-AL}^{r_x=AL}\sum_{r_y=-AL}^{r_y=AL}\tilde{\tilde{D}}^{u_3}(m,n). \tag{13}$$

Finally, the surface deformation is recovered in the spatial domain using the following expression:

$$u_3(x,y) = IFFT\big[\hat{\tilde{D}}^{u_3}(m,n) \circ \hat{p}(m,n)\big], \tag{14}$$

where '$IFFT$' indicates a double inverse fast Fourier transform, '$\circ$' represents element-wise multiplication in the frequency domain, and $\hat{p}$ is the transformed pressure distribution. For computation efficiency, the deformation calculation is performed using the aforementioned DC-FFT technique [40].

2.1.5. Lubricant film temperature

The temperature distribution within the lubricant film is governed by the three-dimensional energy equation for compressible, viscous fluids. Expressed in strong conservation form using compact index notation over the Cartesian coordinates x^n, where $n = \{1,2,3\}$, the governing energy equation is written as follows:

$$\underbrace{\frac{\partial(\rho c T)}{\partial t}}_{\substack{\text{Transient}\\ \text{Term}}} + \underbrace{\frac{\partial}{\partial x^n}(\rho c u_n T)}_{\substack{\text{Convection}\\ \text{Term}}} = \underbrace{\frac{\partial}{\partial x^n}\left(k\frac{\partial T}{\partial x^n}\right)}_{\substack{\text{Conduction}\\ \text{Term}}} + \underbrace{Q_T}_{\substack{\text{Source}\\ \text{Term}}}, \tag{15}$$

$$\text{with,} \quad Q_T = Q_p + Q_c + Q_\Phi + \dot{q}_V,$$

where T is the lubricant temperature, while ρ, c and k represent the lubricant density, specific heat capacity and thermal conductivity, respectively. The fluid velocity components in the three spatial directions are denoted by u_n, and summation over repeated indices is implied according to Einstein notation.

The source term Q_T in Equation 15 incorporates the various thermo-mechanical mechanisms contributing to internal heat generation within the lubricant film. These include compressive heating/cooling associated with pressure variations, enthalpic heating/cooling arising from thermophysical property variations, viscous shear dissipation, and any additional volumetric heat generation mechanisms. The individual contributions are expressed as follows:

$$Q_p = \underbrace{\beta T\left(\frac{\partial p}{\partial t} + u\frac{\partial p}{\partial x} + v\frac{\partial p}{\partial y}\right)}_{\substack{\text{Compressive}\\ \text{Heating/Cooling}}}, \tag{16a}$$

$$Q_c = \underbrace{\rho T\left(\frac{\partial c}{\partial t} + u\frac{\partial c}{\partial x} + v\frac{\partial c}{\partial y} + w\frac{\partial c}{\partial z}\right)}_{\substack{\text{Enthalpic}\\ \text{Heating/Cooling}}}, \tag{16b}$$

$$Q_\Phi = \underbrace{\eta\left[\left(\frac{\partial u}{\partial z}\right)^2 + \left(\frac{\partial v}{\partial z}\right)^2\right]}_{\substack{\text{Shear}\\ \text{Heating}}}. \tag{16c}$$

Additionally, the three-dimensional velocity components of the lubricant film, required for the evaluation of convective heat transport, are expressed as follows:

$$u(x,y,z) = u_1 + \frac{\partial p}{\partial x}\left(\int_{z_1}^{z}\frac{z'dz'}{\eta} - \frac{\eta_e}{\eta'_e}\int_{z_1}^{z}\frac{dz'}{\eta} + \eta_e u_s\int_{z_1}^{z}\frac{dz'}{\eta}\right), \tag{17a}$$

$$v(x,y,z) = v_1 + \frac{\partial p}{\partial y}\left(\int_{z_1}^{z}\frac{z'dz'}{\eta} - \frac{\eta_e}{\eta'_e}\int_{z_1}^{z}\frac{dz'}{\eta} + \eta_e v_s\int_{z_1}^{z}\frac{dz'}{\eta}\right), \tag{17b}$$

$$w(x,y,z) = -\frac{1}{\rho}\frac{\partial}{\partial x}\int_{z_1}^{z}\rho u\, dz' - \frac{1}{\rho}\frac{\partial}{\partial y}\int_{z_1}^{z}\rho v\, dz', \tag{17c}$$

where $u(x,y,z)$, $v(x,y,z)$, and $w(x,y,z)$ denote the lubricant velocity components in the sliding (x-), transverse (y-), and film-thickness (z-) directions, respectively.

2.1.6. Thermal Transport in Solid and Coated Domains

Similar to the thermal treatment of the lubricant film presented in Section 2.1.5, the temperature evolution within the bounding solids and coating layers is governed by transient heat conservation. Internal heat generation within the solid domains is assumed to be negligible relative to the thermal energy generated within the lubricant film and at asperity contact locations. Under this assumption,

thermal transport within the solids is dominated by heat conduction and advection associated with the motion of the contacting bodies.

Using the subscripts $s = 1$ and $s = 2$ to denote the lower and upper contacting solids, respectively, the transient temperature distribution within each solid domain is governed by the following energy equation:

$$\underbrace{\frac{\partial(\rho_s c_s T_s)}{\partial t}}_{\substack{\text{Transient}\\ \text{Term}}} + \underbrace{\frac{\partial}{\partial x^n}(\rho_s c_s v_{n_s} T_s)}_{\substack{\text{Convection}\\ \text{Term}}} = \underbrace{\frac{\partial}{\partial x^n}\left(k_s \frac{\partial T_s}{\partial x^n}\right)}_{\substack{\text{Conduction}\\ \text{Term}}}, \tag{18}$$

where ρ_s, c_s, and k_s represent the density, specific heat capacity, and thermal conductivity of solid body s, respectively. The velocity components of the moving solid domain are denoted by v_{n_s}, where $n = \{1, 2, 3\}$ corresponds to the x-, y-, and z-directions. Equivalently, the solid velocity vector may be expressed as

$$\boldsymbol{v}_s = \begin{bmatrix} u_s & v_s & w_s \end{bmatrix}^T,$$

where u_s, v_s, and w_s denote the velocity components in the sliding, transverse, and out-of-plane directions, respectively.

The same thermal formulation is applied to the coating layers, allowing heat transport within multilayered systems to be resolved consistently with the substrate domains. Consequently, the thermal response of coated interfaces is captured through the coupled solution of the transient energy equations across the lubricant film, coating layers, and solid substrates.

Thermal coupling between adjacent domains is enforced through interfacial heat-flux continuity conditions. At lubricant-solid interfaces, continuity of heat flux requires

$$k \frac{\partial T}{\partial z}\bigg|_{z=z_i} = k_i \frac{\partial T_i}{\partial z}\bigg|_{z=z_i}, \qquad i = \{1, 2\}, \tag{19}$$

where k and k_i denote the thermal conductivities of the lubricant and adjacent solid domain, respectively.

In regions of asperity contact, heat generated by boundary friction is introduced through the solid-solid interfacial heat-flux condition

$$k_1 \frac{\partial T_1}{\partial z}\bigg|_{z=z_1} + k_2 \frac{\partial T_2}{\partial z}\bigg|_{z=z_2} = f_b p_a |u_s|, \tag{20}$$

where f_b is the boundary friction coefficient, p_a is the local asperity contact pressure, and u_s is the relative sliding velocity between the contacting surfaces.

The interfacial temperatures are obtained by enforcing temperature continuity across the coupled domains. Accordingly, the lubricant and solid temperatures are constrained to be equal at fluid-solid interfaces, while equal temperatures are imposed at solid-solid interfaces in regions of asperity contact. This ensures thermodynamic consistency and enables heat transfer between the lubricant, coatings, and contacting solids to be resolved within a unified multiphysics framework.

2.1.7. Interfacial friction

The friction coefficient, μ, is determined from the ratio of the total tangential traction generated within the lubricated interface and the externally applied normal load (W). The total frictional response includes contributions from both viscous shear within the lubricant film and boundary shear arising

from asperity interactions in regions of solid-solid contact. Accordingly, the friction coefficient is expressed as follows:

$$\mu = \frac{\iint_{\Omega} \left(\tau + \tau_a \right) dx\, dy}{W} = \frac{\iint_{\Omega} \left(\eta \frac{\partial u}{\partial z} + f_b p_a \right) dx\, dy}{W}, \tag{21}$$

where Ω denotes the lubricated contact domain over which the tangential tractions are evaluated, and W is the externally applied normal load. The term τ represents the hydrodynamic shear stress generated within the lubricant film, while τ_a corresponds to the asperity shear stress arising from boundary interactions at contacting surface peaks. Here, $\partial u/\partial z$ is the local shear rate normal to the sliding surfaces, p_a is the local asperity contact pressure, and f_b is the boundary friction coefficient.

2.1.8. Constitutive Lubricant Behaviour

The lubricant rheology and thermophysical properties are modelled through pressure-, temperature-, and shear-dependent constitutive relationships in order to capture the strongly coupled behaviour arising under severe lubrication conditions. In particular, variations in viscosity and density are incorporated directly into the governing equations, enabling the influence of thermal effects, compressibility, and non-Newtonian shear response on the hydrodynamic and thermal fields to be resolved consistently.

The pressure-temperature dependence of the lubricant dynamic viscosity is described using the classical Roelands equation formulation, expressed as follows [42]:

$$\eta = \eta_0 \exp\left\{ \left[\ln \eta_0 + 9.67 \right] \times \left[(1 + 5.1 \times 10^{-9} p)^z \times \left(\frac{T - 138}{T_0 - 138} \right)^{-s} - 1 \right] \right\}, \tag{22}$$

where

$$z = \frac{\alpha_p}{5.1 \times 10^{-9} (\ln \eta_0 + 9.67)}, \qquad s = \frac{0.0476 (T_0 - 138)}{\ln \eta_0 + 9.67},$$

using the pressure-viscosity coefficient α_p and the reference (or ambient) temperature T_0. Here, η_0 denotes the reference lubricant viscosity at T_0, while α_p is the pressure-viscosity coefficient. This formulation enables the strong pressure-induced viscosity growth and thermal viscosity reduction characteristic of concentrated lubricated contacts to be represented accurately.

To account for non-Newtonian behaviour under high shear conditions, the Eyring model shear-thinning model is employed [43]:

$$\dot{\gamma} = \frac{\tau_E}{\eta} \sinh\left(\frac{\tau}{\tau_e} \right), \tag{23}$$

where $\dot{\gamma}$ is the shear rate, τ is the shear stress, and τ_E is the Eyring shear stress, taken in the present study as 10 MPa. The Eyring formulation enables the reduction in effective viscosity at high shear rates to be captured, thereby providing a more realistic representation of lubricant behaviour in heavily loaded and high-sliding contacts.

Furthermore, the pressure-temperature dependence of the lubricant density is described using the Dowson-Higginson empirical relationship as follows [44,45]:

$$\rho = \rho_0 \left(1 + \frac{0.6 \times 10^{-9} p}{1 + 1.7 \times 10^{-9} p} \right) \left[1 - 0.00065 \times (T - T_0) \right], \tag{24}$$

where ρ_0 is the reference density at ambient conditions, taken in the present study as 980 kg/m^3.

2.2. Case studies

2.2.1. Case study 1 - Transient starvation with roughness

To demonstrate the capabilities of the proposed framework, two case studies were considered. The first case study focused on transient starvation in the presence of surface roughness, with particular emphasis on the resulting thermo-mechanical response of the contact. The analysis began with a smooth, fully flooded EHL contact, which served as a reference state. Starvation was then imposed at the inlet boundary and its transient propagation through the contact was simulated. This allowed the evolution of key quantities, such as film thickness reduction and coefficient of friction, to be systematically evaluated as the lubricant supply decreased and the system transitioned towards a starved steady state. Starvation was imposed by setting the value of h_{oil} at the inlet, $h_{oil}(x_{in}, y)$, to $0.25 \cdot h_{c,ff}$, where $h_{c,ff}$ is the central film thickness at fully-flooded conditions. The value of $h_{c,ff}$ in case study 1 was 25 nm.

Once the baseline response for the smooth starved contact was established, deterministic surface roughness was introduced in the form of isotropic sinusoidal features on the upper surface only travelling through the contact. The lower surface was smooth. Three different wavelengths ($\omega = 200$ μm, 100 μm and 50 μm) were considered in order to investigate the influence of surface topography on the contact behaviour, while the roughness amplitude, A, was fixed at 0.1 μm. This approach allowed the effect of roughness scale on film formation and thermal response to be systematically assessed.

The dimensional profile of the upper surface, containing the travelling isotropic sinusoidal features, is defined as

$$s_2(x, y, t) = A\left[\cos\left(2\pi \cdot \frac{x - x_d}{\omega}\right) \cdot \cos\left(2\pi \cdot \frac{y}{\omega}\right)\right],$$

where A is the amplitude of the roughness profile, ω is the wavelength of the roughness profile, $x_d = (x_s + u_2 t)$ is the position of the roughness profile in the domain and x_s is the position of the roughness profile at $t = 0$.

To promote asperity interactions and enhance the resulting thermal effects, a relatively low lubricant viscosity (η_0 = 0.01 Pa·s) was employed. In addition, an asperity friction coefficient, f_b, of 0.2 was used in order to emphasise flash temperature generation at asperity contacts. This combination of parameters ensured that mixed lubrication conditions are achieved, allowing the coupled effects of starvation, roughness and asperity heating to be clearly observed. A summary of all the input parameters used is found in Table 1 below.

Table 1. Input parameters for case study 1.

Parameter type	Parameter	Value
Operating conditions	Applied load, W [N]	100
	Entrainment speed, u_{ent} [m/s]	0.25
	Slide-to-roll ratio, SRR [-]	2
	Reference temperature, T_0 [°C]	20
Solid properties	Effective radius of curvature, R [mm]	19.05
	Young's modulus of solid bodies, $E_{1,2}$ [GPa]	210
	Poisson's ratio of solid bodies, $\nu_{1,2}$ [-]	0.3
	Thermal conductivity of solid bodies, $k_{1,2}$ [W/(m·K)]	21
	Specific heat capacity of solid bodies, $c_{1,2}$ [J/(kg·K)]	446
	Density of solid bodies, $\rho_{1,2}$ [kg/m^3]	7710
Lubricant properties	Lubricant reference viscosity, η_0 [Pa·s]	0.01
	Lubricant pressure-viscosity coefficient, α_p [GPa^{-1}]	18.2
	Fluid specific heat capacity, c [J/(kg·K)]	1867
	Fluid thermal conductivity, k [W/(m·K)]	0.104
	Fluid coefficient of thermal expansion, β [1/K]	8.36×10^{-4}
	Eyring shear stress, τ_E [MPa]	10
	Reference density, ρ_0 [kg/m^3]	980
Simulation parameters	Mesh size for fluid and solid domains, $N_x \times N_y \times N_z$	$128 \times 128 \times 11$
	Computational domain	$-2.5 \leq x/a \leq 2$, $-2 \leq y/a \leq 2$ *
	Solids thickness, D_S [m]	$3.15 \cdot a$
	Dimensional time step, dt [s]	$dt = dx/u_{ent}$
	Cavitation pressure, p_{cav} [kPa]	100
	Pressure-liquid film fraction convergence criterion, $e^{p,\theta}$	1×10^{-5}
	Load convergence criterion, e^W	1×10^{-4}
	Temperature convergence criterion, e^T	1×10^{-4}
	Global pressure convergence criterion, e^p_{global}	1×10^{-3}
	Global temperature convergence criterion, e^T_{global}	1×10^{-3}

*$a = [3WR/(2E')]^{1/3}$ is the Hertzian contact radius.

2.2.2. Case study 2 - Transient starvation with coatings

The second case study aims to highlight the influence of surface coatings on the transient response of a system subjected to starvation. The same baseline operating conditions as in case study 1 were employed to ensure consistency, with the exception of a higher entrainment speed of 1 m/s. Also, in this case only smooth surfaces were considered in order to isolate the effect of coating properties from surface roughness.

As in case study 1, starvation was imposed at the inlet boundary by prescribing a reduced inlet oil layer thickness of $0.25 \cdot h_{c,ff}$, with the value of $h_{c,ff}$ in case study 2 being 80 nm. The resulting evolution of film thickness, temperature and frictional response was then analysed.

To investigate the effect of coating thermal properties, three coatings with different thermal inertia values were considered. According to Habchi [19], thermal inertia is a metric which describes the ability of a material to transport heat by conduction and advection. This is defined as $TI = \sqrt{k\rho c}$. A material with high thermal inertia has a high ability to transport heat by conduction and advection while a material with low thermal inertia has a low ability to do so, thus it acts as an insulator.

The properties of the three coatings used in this study are summarised in Table 2 below. All three coatings have the same mechanical properties as the solid substrates as outlined in in Table 1. Furthermore, all three coatings have the same thickness ($h_{coating}$) of 40 μm and they are applied to the surface of both top and bottom substrates. Lastly, the coating denoted 'Regular TI' also has the same thermal properties as the solid bodies.

Table 2. Coating thermal properties

	Coating		
Parameter	Low TI	Regular TI	High TI
Thermal conductivity, $k_{c1,2}$ [W/(m·K)]	5	21	90
Specific heat capacity, $c_{c1,2}$ [J/(kg·K)]	200	446	1000
Density, $\rho_{c1,2}$ [kg/m^3]	3500	7710	10000

3. Results

3.1. Model validation

3.1.1. Deterministic treatment of roughness

To validate the accuracy of the deterministic model under isothermal conditions, results were compared with those of Venner and Lubrecht [46] who investigated the influence of a transverse ridge moving over a smooth surface on the film thickness and pressure profiles in a circular EHL contact under rolling/sliding conditions. The authors conducted all simulations using a Newtonian viscosity model.

The dimensional profile of the upper surface, where the transverse ridge is located and which moves in the domain with time, is defined using the following equation.

$$s_2(x,y,t) = \left(\frac{a^2}{R}\right)\overline{A} \times 10^{-10\left(\frac{X-X_d}{\mathbb{W}}\right)^2} \cos\left(2\pi\frac{X-X_d}{\overline{\omega}}\right)$$

where $\overline{A}$ is the dimensionless amplitude of the ridge, $\overline{\omega}$ is the dimensionless wavelength of the ridge, $X_d = (x_s + u_2 t)/a$ is the dimensionless position of the ridge in the domain and x_s is the position of the ridge at $t = 0$.

The authors used a second-order scheme for the discretisation of the entraining and squeeze flow terms in the Reynolds equation and conducted a brief accuracy analysis comparing the effect of the discretisation scheme on the film thickness.

In Figures 2 and 3, pressure and film thickness profiles at different simulation time values (hence different values of X_d) are presented for $SRR = 1$ (simple sliding, smooth surface moves faster than rough surface) and $SRR = -2$ (simple sliding, stationary smooth surface), respectively.

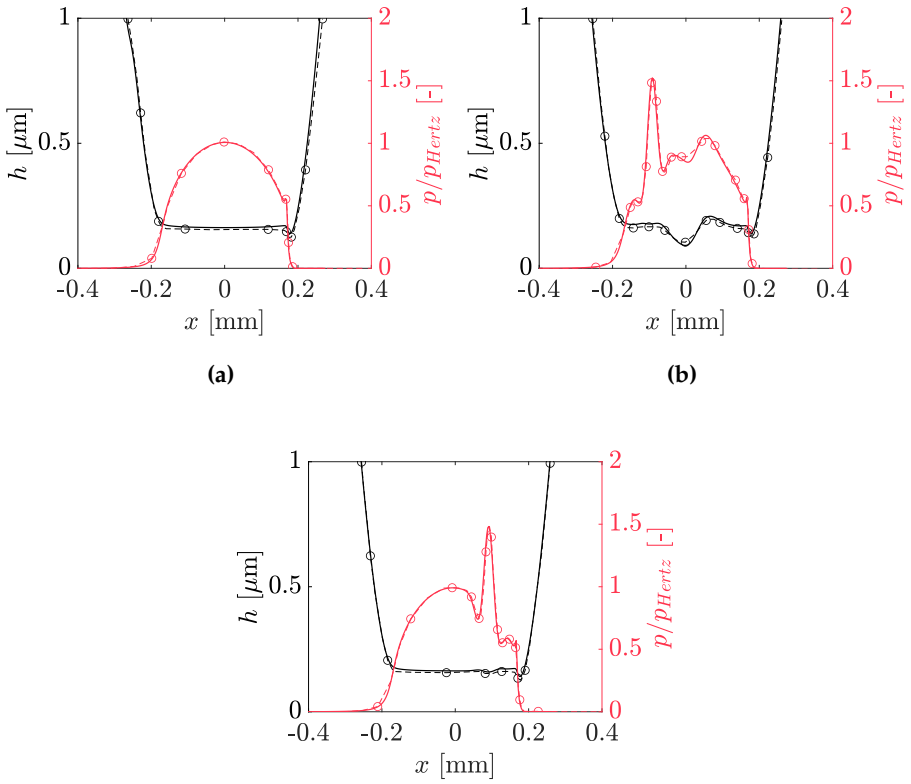

Figure 2. Centreline pressure and film thickness profiles with surface feature (ridge) at **(a)** $X_d = -1.50$, **(b)** $X_d = -0.50$ and **(c)** $X_d = 0.50$ for $SRR = 1$. Dashed lines with markers show results of Venner and Lubrecht [46].

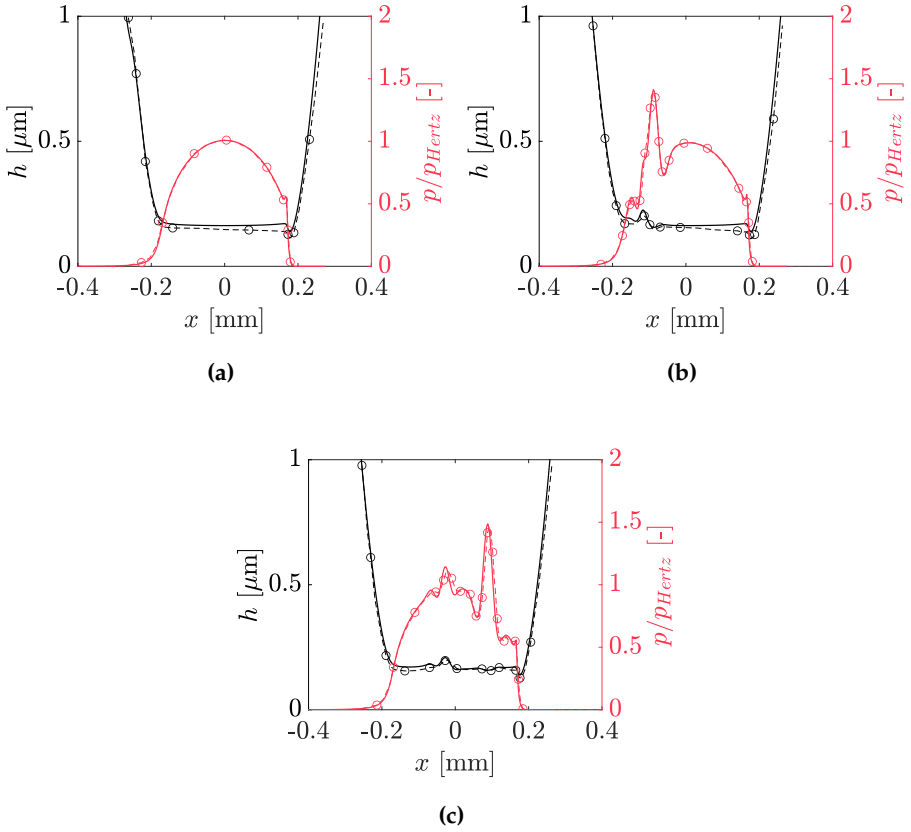

Figure 3. Centreline pressure and film thickness profiles with surface feature (ridge) at **(a)** $X_d = -1.50$, **(b)** $X_d = -0.50$ and **(c)** $X_d = 0.50$ for $SRR = -2$. Dashed lines with markers show results of Venner and Lubrecht [46].

For both SRR values, the current model shows excellent agreement with the results in [46]. Quantitatively, for $SRR = 1$, the root mean square error (RMSE) values for the normalised pressure distributions are in the range of 2.2×10^{-2} to 3.4×10^{-2}, while for the film thickness profiles the RMSE values are between 1.3×10^{-2} and 4.2×10^{-2} μm across the different time instances considered. Similarly, for $SRR = -2$, the pressure RMSE values range from 1.9×10^{-2} to 7.5×10^{-2}, while the film thickness RMSE values range from 2.6×10^{-2} to 5.2×10^{-2} μm. It should be noted that the reference data used for the RMSE calculations were obtained by digitising the published figures in [46], which may introduce minor uncertainties associated with the extraction procedure. Moreover, certain numerical parameters required to exactly reproduce the results of Venner and Lubrecht are not explicitly specified in their paper. In particular, the convergence criterion of the EHL solver and the value of the pressure-viscosity coefficient exponent in the Roelands viscosity equation are not reported. In the present work, an EHL solver convergence criterion of 10^{-5} was used. Furthermore, a value of 0.6 was used for the pressure-viscosity coefficient exponent in the Roelands viscosity equation, consistent with the recommendation provided by Venner and Lubrecht in another study [47]. Despite the above, the low error magnitudes demonstrate that the present model is able to accurately reproduce the transient behaviours reported by Venner and Lubrecht.

In addition to the quantitative agreement, the model also reproduces the characteristic transient pressure and film thickness responses associated with moving surface features. According to Ai and Cheng [48], when the surface feature moves at a speed slower than the entrainment speed (Figure 2), the pressure ridge and surface indentation occur on the leading side and extend in front of the surface feature, whereas when the surface feature moves at a speed faster than the entrainment speed (Figure 3), a pressure ridge is formed at the trailing edge.

Further validation of the transient deterministic model was performed, comparing with the results of Cui et al. [49] who investigated the influence of two rough surfaces with transverse ridges moving against each other at different speeds. In contrast to the study by Venner and Lubrecht [46], Cui et al. [49] conducted all simulations under transient thermal conditions.

Figure 4 presents the evolution of centreline pressure and film thickness profiles at selected time iterations, while Figure 5 shows the corresponding mid-film and solid temperature distributions.

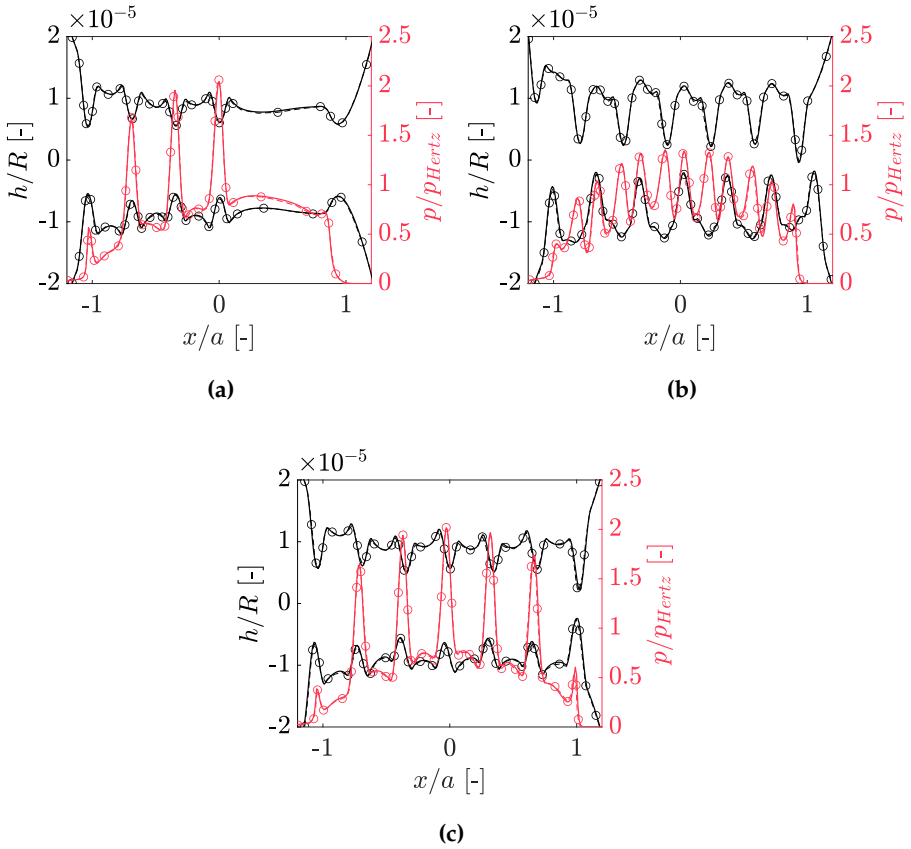

Figure 4. Centreline pressure and film thickness profiles with surface features (ridges) at time iteration **(a)** $N = 700$, **(b)** $N = 1024$ and **(c)** $N = 1043$. Dashed lines with markers show results of Cui et al. [49].

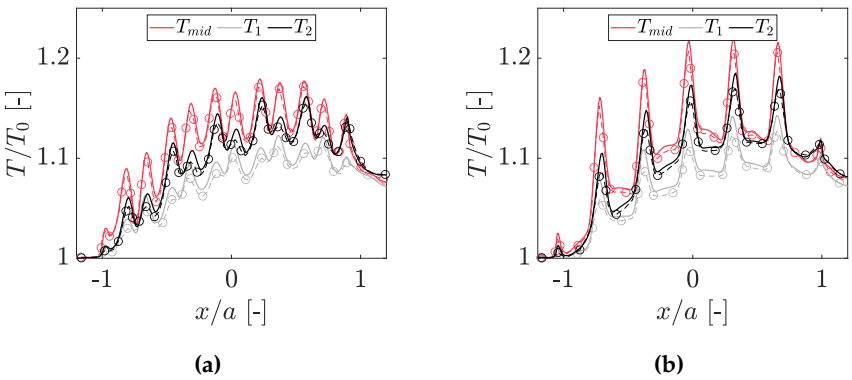

Figure 5. Centreline mid-film and solid temperature profiles with surface features (ridges) at time iteration **(a)** $N = 1024$ and **(b)** $N = 1043$. Dashed lines with markers show results of Cui et al. [49].

The agreement with the results of Cui et al. is excellent. Quantitatively, the RMSE values for the normalised pressure distributions are between 2.9×10^{-2} and 5.6×10^{-2} across the three considered

time instances. Similarly, the dimensionless upper and lower surface film thickness profiles exhibit RMSE values of the order of 10^{-7}. These low error magnitudes demonstrate that the model accurately captures the transient interaction of surface features and the resulting hydrodynamic response.

Similarly, very good agreement is observed for the temperature profiles in both the lubricant and solid domains. The dimensionless temperature RMSE values are of the order of 10^{-3} for the mid-film and solid temperatures at both considered time instances, confirming that the model accurately captures the overall shape and evolution of the temperature distributions, including the localised temperature rise associated with ridge interaction.

A slight deviation in the magnitude of the predicted temperatures can be attributed to the fact that the spacing of the nodes of the solid domain in the thickness (z) direction is not specified in [49]. In the present work, a non-uniform grid based on cosine spacing was employed to better resolve steep temperature gradients near the fluid-solid interface.

Additional simulations were carried out to assess the influence of the spacing of the nodes in the solids on the temperature field. These confirmed that the predicted temperature levels are sensitive to the node distribution in the solid, while the overall trends and spatial distributions remain unaffected.

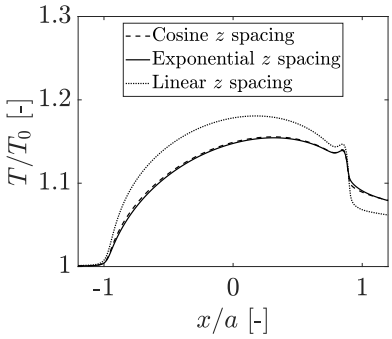

Figure 6. Centreline mid-film temperature profiles for different z-direction node spacings in the solids.

3.1.2. Surface coatings

To validate the accuracy of the surface coatings model, results were compared with those of Habchi [19] who investigated the influence of the mechanical and thermal properties of surface coatings on the pressure and film thickness profiles of a coated circular contact. To investigate the effect of the coatings' mechanical properties, the authors independently varied the coatings' thickness and Young modulus values. To investigate the effect of the coatings' thermal properties, the authors varied the coatings' thermal inertia (TI).

Figure 7 shows the effect of the coatings' mechanical properties on the pressure and film thickness profiles. To study the effect of coating Young modulus, a coating thickness of 40 μm was used and to study the effect of coating thickness two different values for coating Young modulus were used: 105 GPa and 420 GPa.

Figure 8 shows the effect of the coatings' thermal properties, namely TI, on the mid-film temperature profiles at two different applied loads, 25 and 100 N. Figure 9 shows the effect of the coatings' TI on the temperature profiles across the z-direction for an applied load of 100 N.

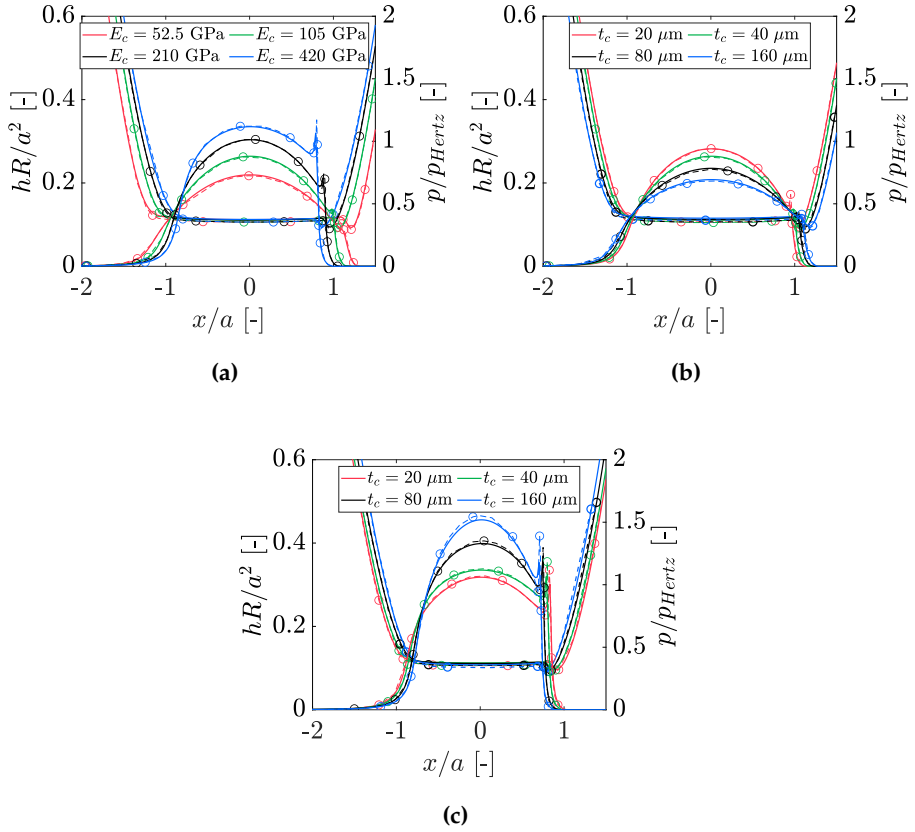

Figure 7. Centreline pressure and film thickness profiles for coatings with different mechanical properties. **(a)** Variation of coating Young Modulus ($t_c = 40$ μm). **(b)** Variation of coating thickness (Soft coating - $E_c = 105$ GPa). (c) Variation of coating thickness (Hard coating - $E_c = 420$ GPa). Dashed lines with markers show results of Habchi [19].

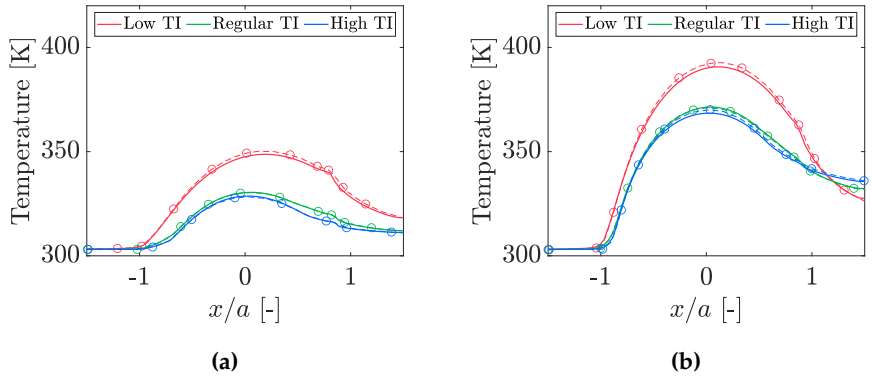

Figure 8. Centreline mid-film temperature profiles for coatings with different thermal inertia (TI) values at applied loads of **(a)** 25 N and **(b)** 100 N. Dashed lines with markers show results of Habchi [19].

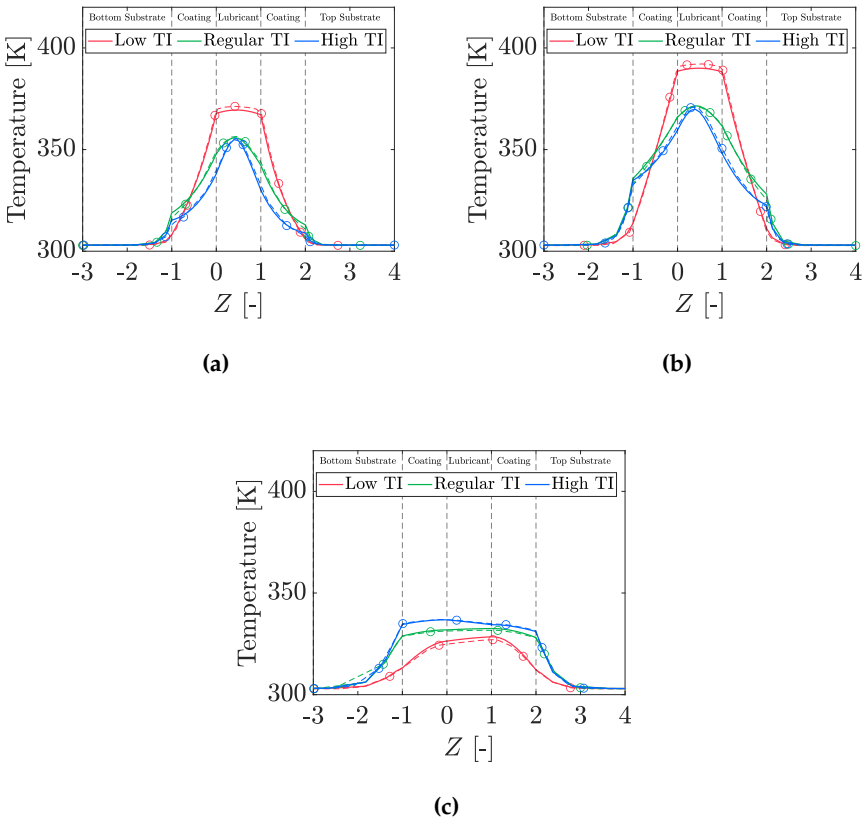

Figure 9. Centreline temperature profiles across z for coatings with different thermal inertia (TI) values at **(a)** $x/a = -0.5$, **(b)** $x/a = 0$ and **(c)** $x/a = 1.5$ for an applied load of 100 N. Dashed lines with markers show results of Habchi [19].

Overall, excellent agreement is also observed with the results of Habchi. The predicted pressure and film thickness profiles closely match the reference results for all considered coating configurations, accurately capturing the influence of both coating thickness and Young's modulus on the contact behaviour, with RMSE values for the film thickness profiles of the order of 10^{-3} and RMSE values for the pressure profiles of the order of 10^{-2}.

Similarly, very good agreement is obtained for the thermal results, with the maximum temperature RMSE value being 1.53 K occurring for the low TI mid-film temperature profiles at an applied load of 100 N. The model successfully captures the influence of coating thermal inertia on the temperature distributions, including the variation in mid-film temperature and the distribution of temperature across the z-direction. The trends associated with both high and low thermal inertia coatings are well reproduced, confirming that the heat transfer within the coated system is accurately resolved.

Despite the use of a different numerical formulation (semi-system vs Habchi's full-system), the close agreement observed in both mechanical and thermal responses demonstrates the robustness and accuracy of the present approach for modelling coated EHL contacts.

3.2. Case study 1

Figure 10 shows the evolution of key parameters with dimensionless time for the duration of the simulations as the starvation front and subsequently the roughness profiles move through the computational domain. In total, the simulation consisted of 800 time iterations (N), covering a dimensionless time, $\bar{t}$, of 28.31. Iteration 1 was a fully-flooded smooth case. From iteration 2 onwards, starvation was imposed at the inlet. Once the starvation front had moved through the contact and a steady state had been reached, a roughness profile started moving through the contact at $N = 501$.

The maximum temperature rise values were calculated by subtracting the temperatures at asperity contact locations from the corresponding temperatures at those locations before the roughness profiles enter the contact at a time when the system is at steady state. In this case, the reference temperatures were taken at $\bar{t} = 17.68$ ($N = 500$). The coefficient of friction (COF) presented is the average value of the COF calculated at the top and bottom surfaces. The z-coordinate in case study 1 was normalised in the following way:

- Lower solid: $Z = z/a$ $\{-3.15, 0\}$
- Fluid: $Z = z/h$ $\{0, 1\}$
- Upper solid: $Z = z/a$ $\{1, 4.15\}$

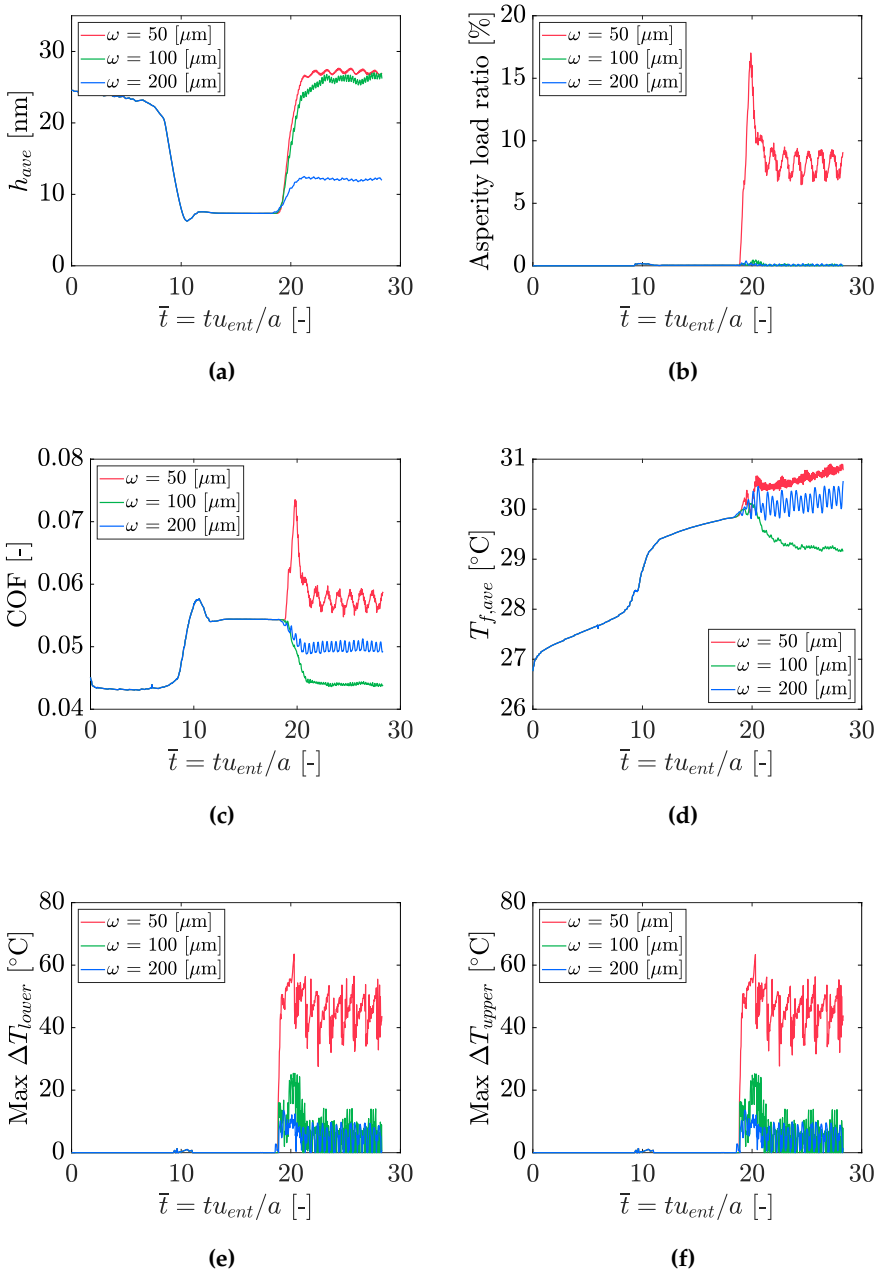

Figure 10. Variations of **(a)** average film thickness in Hertzian region, **(b)** asperity load ratio, **(c)** coefficient of friction, **(d)** average fluid temperature and maximum temperature rise at asperity contact locations at **(e)** lower and **(f)** upper surfaces with dimensionless time.

Figures 11-13 show contour plots of oil film thickness (h_{oil}), liquid film fraction (θ) and temperature across the z-direction across both fluid and solid domains, respectively, at different time iterations as the starvation front is moving through the contact.

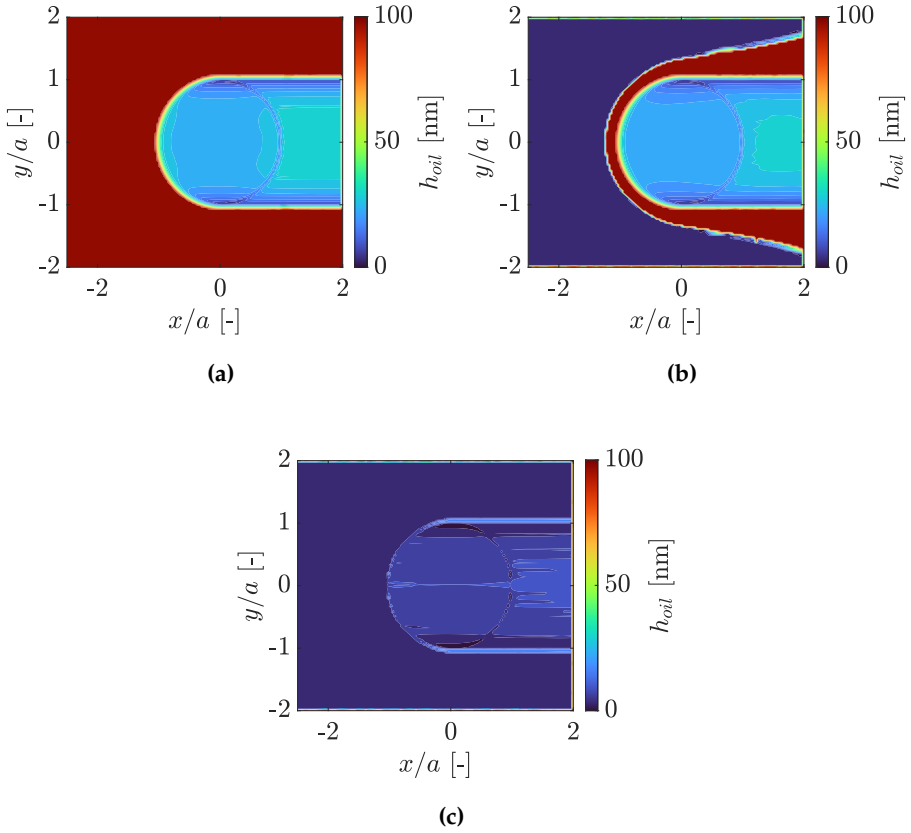

Figure 11. Contour plot of oil film thickness (h_{oil}) at **(a)** $\bar{t} = 0$ ($N = 1$), **(b)** $\bar{t} = 7.05$ ($N = 200$) and **(c)** $\bar{t} = 14.14$ ($N = 400$).

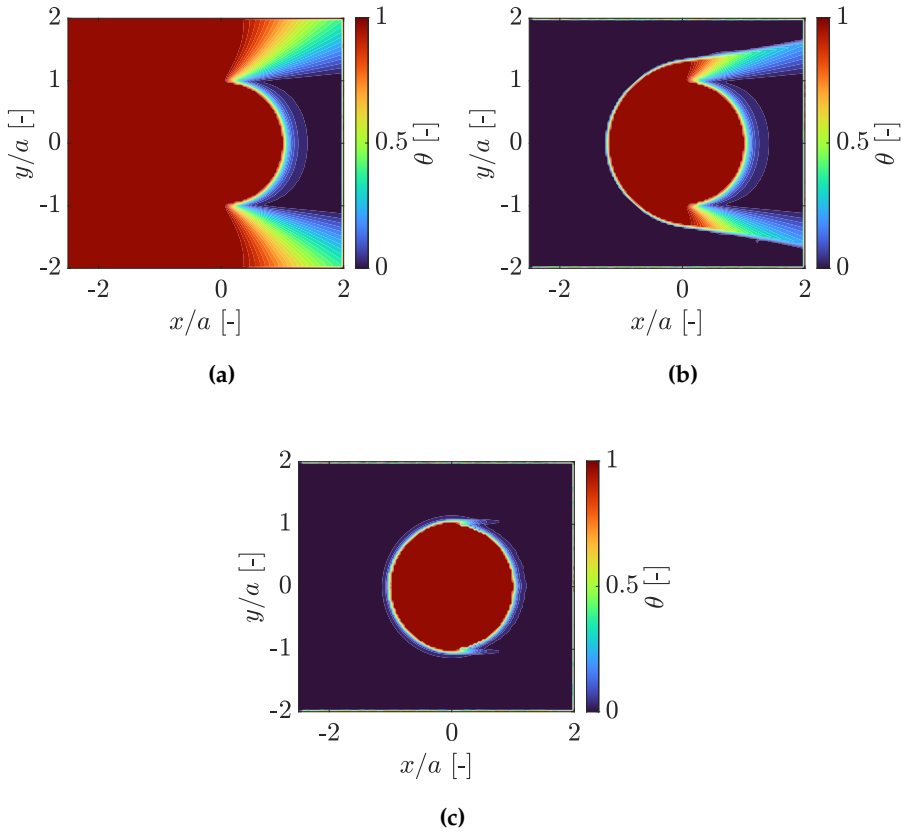

Figure 12. Contour plot of liquid film fraction (θ) at **(a)** $\bar{t} = 0$ ($N = 1$), **(b)** $\bar{t} = 7.05$ ($N = 200$) and **(c)** $\bar{t} = 14.14$ ($N = 400$).

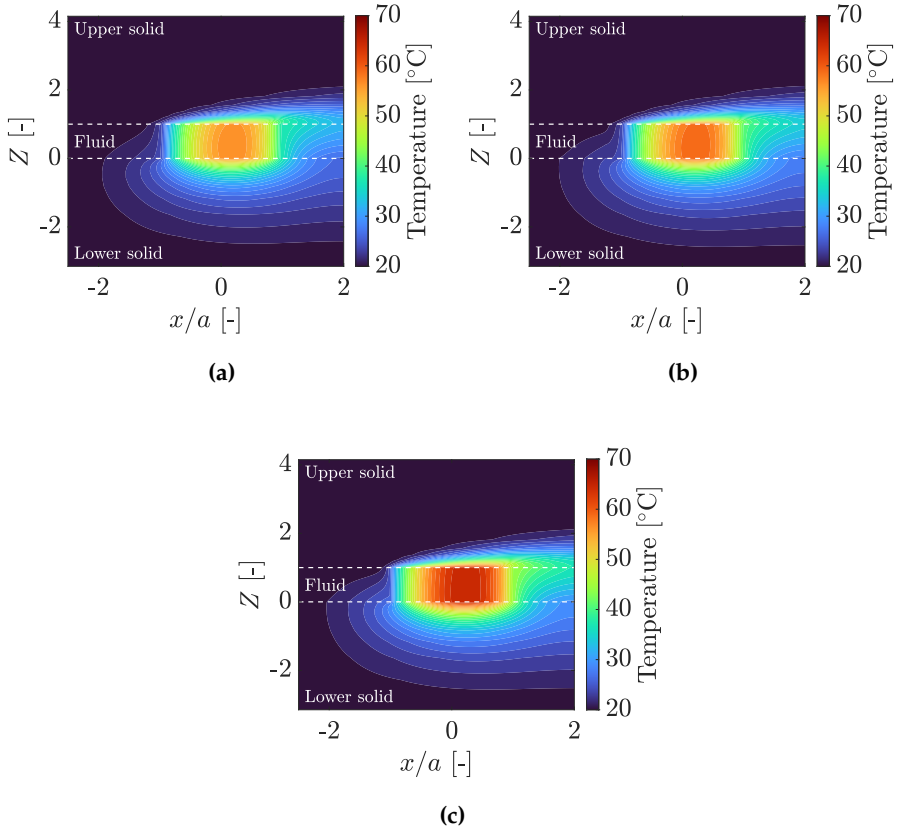

Figure 13. Contour plot of temperature across z ($y = 0$) at **(a)** $\bar{t} = 0$ ($N = 1$), **(b)** $\bar{t} = 7.05$ ($N = 200$) and **(c)** $\bar{t} = 14.14$ ($N = 400$).

Figures 14-16 show contour plots of oil film thickness (h_{oil}), liquid film fraction (θ) and temperature across the z-direction across both fluid and solid domains, respectively, at $\bar{t} = 21.22$ ($N = 600$) for the three different roughness profiles.

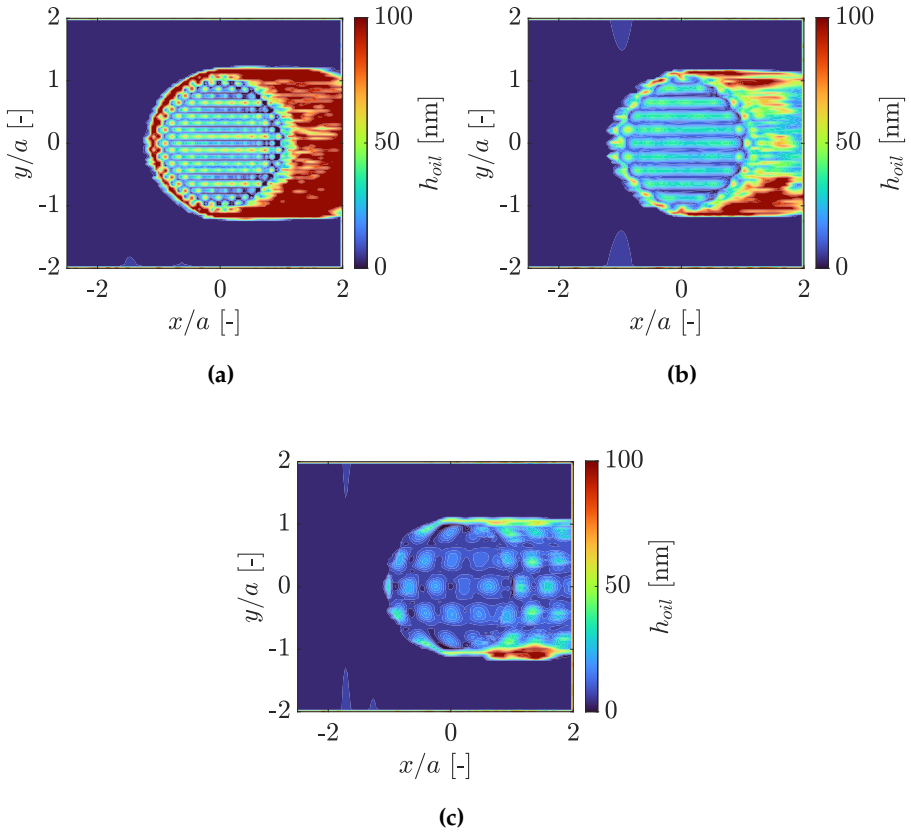

Figure 14. Contour plot of oil film thickness (h_{oil}) at $\bar{t} = 21.22$ ($N = 600$) for roughness profiles with **(a)** $\omega = 50$ μm, **(b)** $\omega = 100$ μm and **(c)** $\omega = 200$ μm.

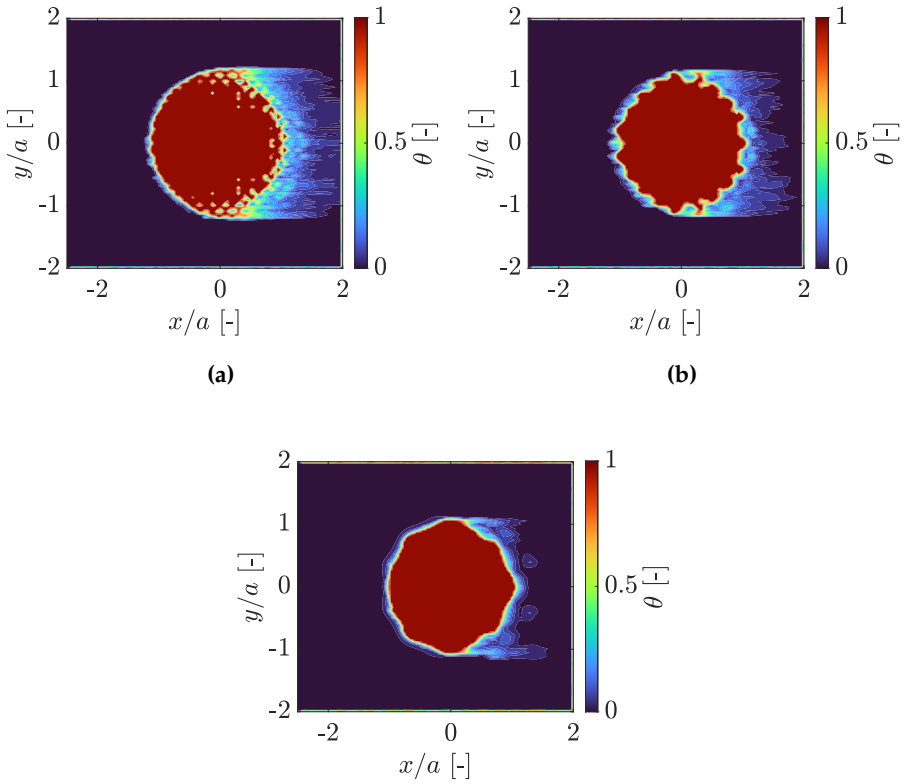

Figure 15. Contour plot of liquid film fraction (θ) at $\bar{t} = 21.22$ ($N = 600$) for roughness profiles with **(a)** $\omega = 50$ μm, **(b)** $\omega = 100$ μm and **(c)** $\omega = 200$ μm.

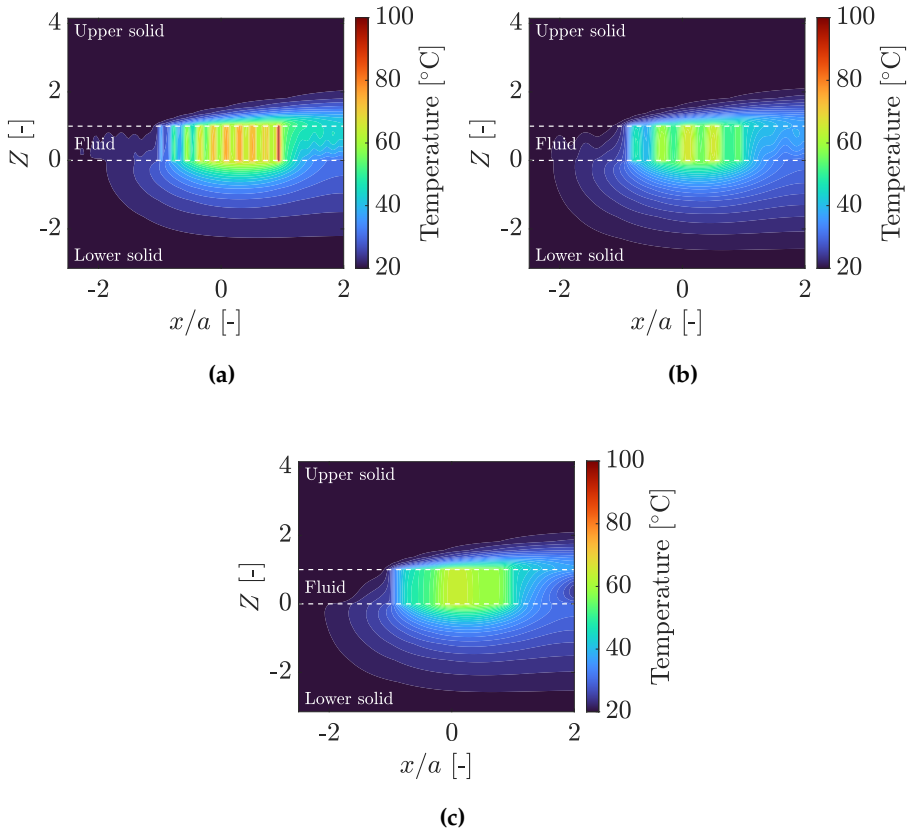

Figure 16. Contour plot of temperature across z ($y = 0$) at $\bar{t} = 21.22$ ($N = 600$) for roughness profiles with **(a)** $\omega = 50$ μm, **(b)** $\omega = 100$ μm and **(c)** $\omega = 200$ μm.

3.3. Case study 2

Figure 17 shows the evolution of key parameters with dimensionless time for the duration of the simulations as the starvation front moves through the computational domain. In total, the simulation consisted of 500 time iterations, covering a dimensionless time, $\bar{t}$, of 17.68. As was the case in case study 1, iteration 1 was a fully-flooded smooth case. From iteration 2 onwards, starvation was imposed at the inlet. The z-coordinate in case study 2 was normalised in the following way:

- Lower solid: $Z = z/a$ $\{-4.15, -1\}$
- Lower coating: $Z = z/h_{coating}$ $\{-1, 0\}$
- Fluid: $Z = z/h$ $\{0, 1\}$
- Upper coating: $Z = z/h_{coating}$ $\{1, 2\}$
- Upper solid: $Z = z/a$ $\{2, 5.15\}$

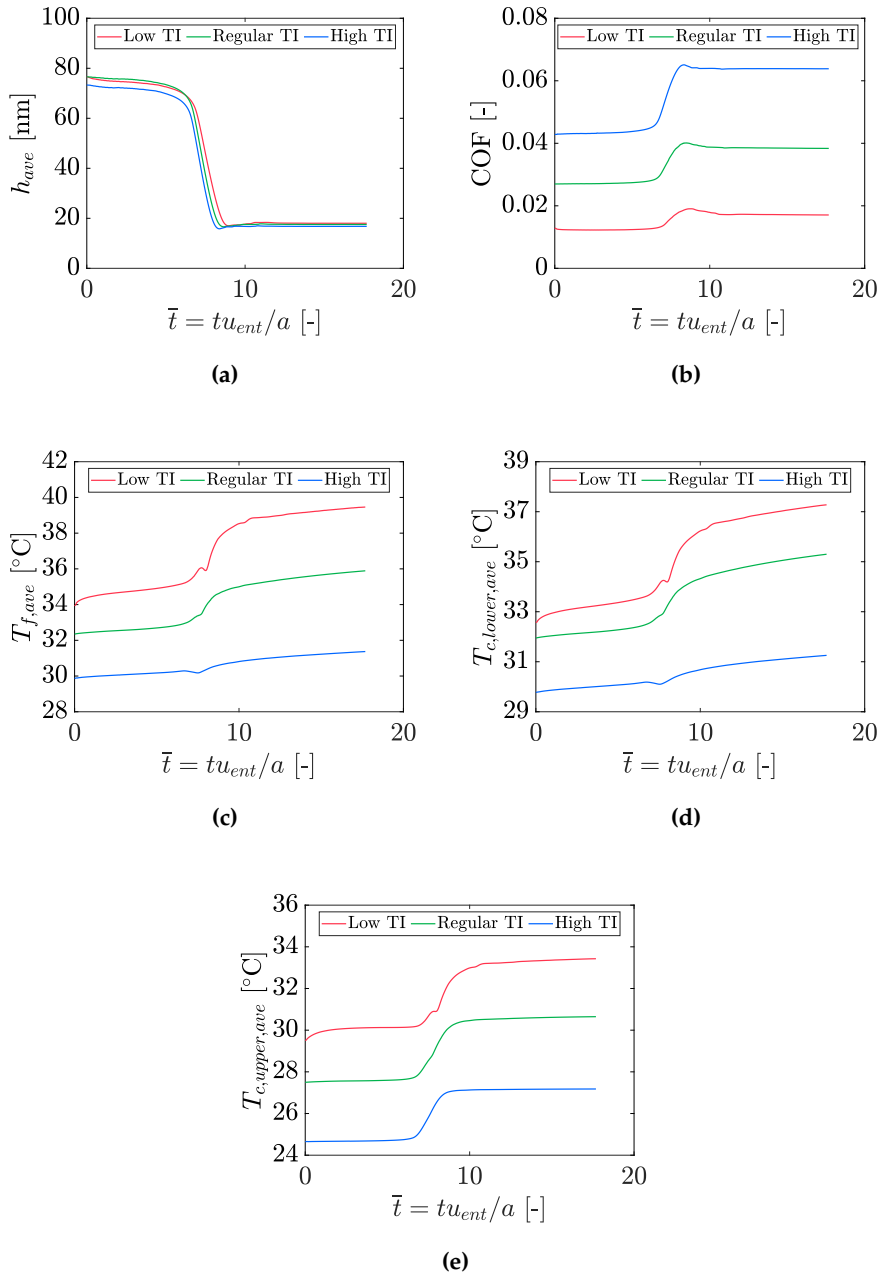

Figure 17. Variations of **(a)** average film thickness in Hertzian region, **(b)** coefficient of friction, **(c)** average fluid temperature, **(d)** average lower coating temperature and **(e)** average upper coating temperature with dimensionless time for three different coatings.

Figure 18 shows line plots of temperature across the z-direction across both fluid, coating and solid domains for the systems with the different coatings at three time iterations. Figures 19 and 20 show contour plots of temperature across the z-direction across both fluid, coating and solid domains for the systems with the different coatings before and after starvation, respectively.

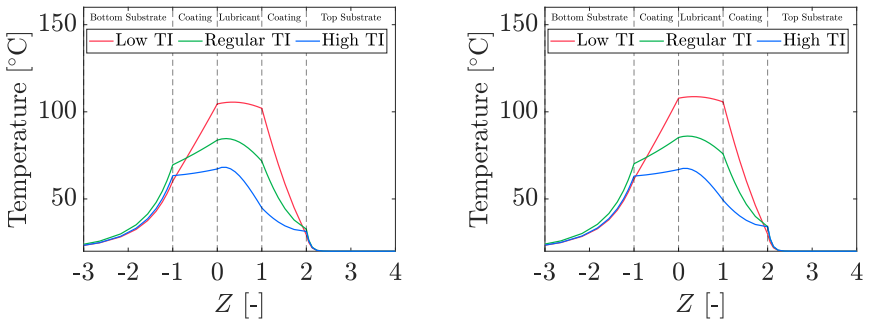

(a) **(b)**

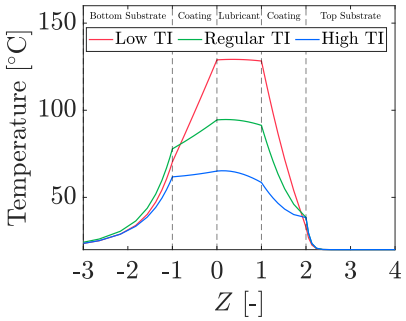

(c)

Figure 18. Line plots of temperature across z ($x = y = 0$) at **(a)** $\bar{t} = 0$ ($N = 1$), **(b)** $\bar{t} = 7.05$ ($N = 200$) and **(c)** $\bar{t} = 14.14$ ($N = 400$) for three different coatings.

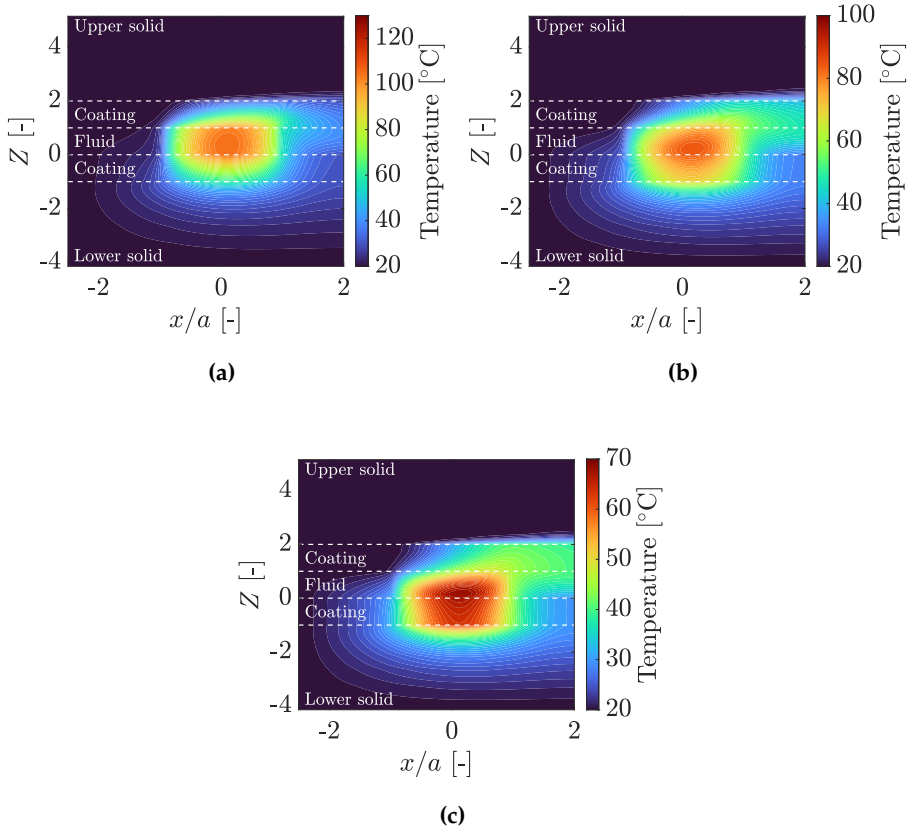

Figure 19. Contour plot of temperature across z ($y = 0$) at $\bar{t} = 0$ ($N = 1$) for system with **(a)** Low TI, **(b)** Regular TI and **(c)** High TI coatings.

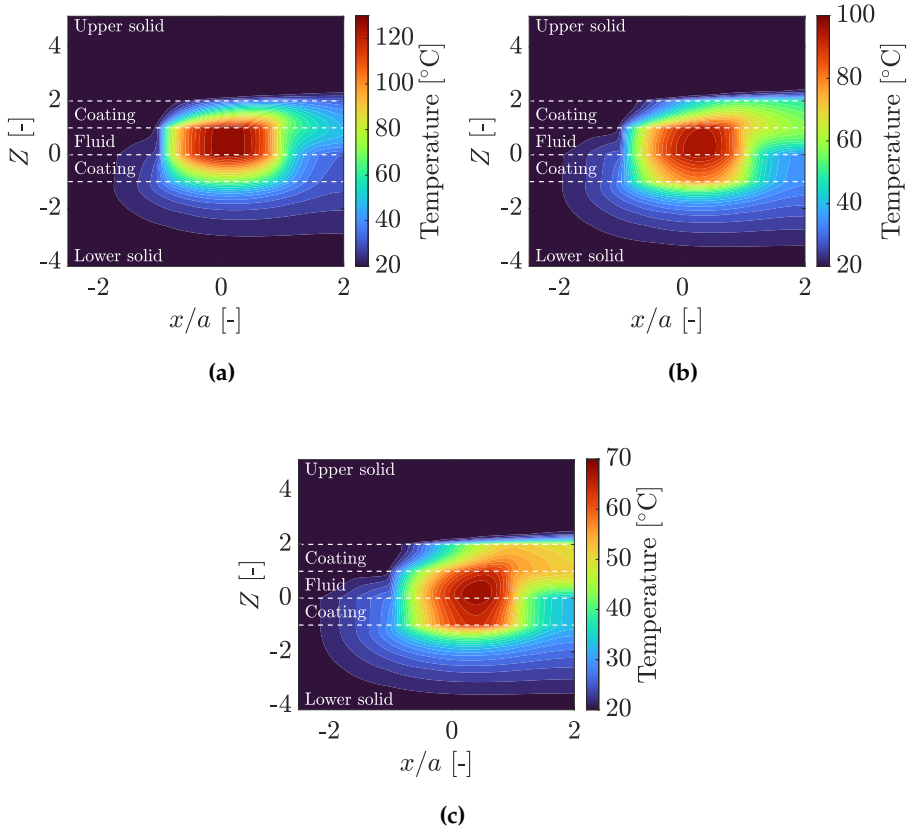

Figure 20. Contour plot of temperature across z ($y = 0$) at $\bar{t} = 14.14$ ($N = 400$) for system with **(a)** Low TI, **(b)** Regular TI and **(c)** High TI coatings.

4. Discussion

4.1. Case study 1

Figure 10 shows that the transient response of the system can be divided into four distinct phases.

Phase 1, covering $\bar{t} \approx 0 - 10$, corresponds to the propagation of the starvation front from the inlet towards the Hertzian contact region. During this phase, the lubricant supply progressively decreases, leading to a reduction in film thickness as the inlet conditions begin to influence the contact. As the film becomes thinner, the shear rate within the lubricant increases, resulting in a gradual rise in the friction coefficient and fluid temperature. When the starvation front reaches the Hertzian zone, a sharp drop in film thickness is observed, accompanied by a sudden increase in temperature due to increased viscous heating. A brief occurrence of asperity contact may be observed at this point, but this is transient and the contact rapidly returns to full-film conditions.

As seen in Figures 11 and 12 the starvation front moves faster at the edges of the contact than at the centre. The pressure is consistently higher along the centreline of the contact and decreases towards the edges. Hence, as the starvation front propagates and the lubricant supply is reduced, the pressure in the outer regions of the contact drops below the cavitation pressure earlier than at the centre. This leads to the onset of cavitation at the edges, with the central region remaining pressurised for longer, giving rise to the observed 'engulfing' behaviour of the starvation front.

Phase 2, covering $\bar{t} \approx 10 - 19$, corresponds to a starved steady state being reached for smooth solid surfaces. The film thickness stabilises at a reduced level governed by the inlet oil layer thickness and the friction coefficient correspondingly reaches a steady value. In contrast, the temperature continues to increase gradually during this phase, indicating a lag in the thermal response relative to the hydrodynamic behaviour. This is attributed to the time required for heat generated within the

lubricant film to diffuse into the surrounding solid domains, leading to a delayed approach to thermal equilibrium.

Figure 13 further illustrates the effect of starvation on the temperature distribution across the film thickness. As already mentioned, starvation leads to an overall increase in fluid temperature due to enhanced viscous heating under reduced film thickness. In addition, a noticeable change in the thermal profile across the film is observed. Under fully flooded conditions, the temperature distribution is asymmetric, with higher temperatures near the stationary lower surface and lower temperatures near the moving upper surface. However, at starved conditions, the temperature distribution becomes significantly more uniform across the film thickness, with reduced thermal gradients between the two surfaces. This behaviour is primarily attributed to the reduced film thickness, which promotes a more uniform shear and heat generation within the lubricant layer.

Phase 3, covering $\bar{t} \approx 19 - 25$, begins with the introduction of the deterministic roughness profiles into the starved contact. The roughness profiles enter the domain after $\bar{t} = 17.68$ and propagate through the contact, reaching the centre of the Hertzian zone at $\bar{t} = 19.45$. Three different isotropic sinusoidal profiles were considered, with wavelengths $\omega = 50, 100$ and 200 μm, and with each case exhibiting a different thermo-mechanical response.

Across all cases, the arrival of the roughness front induces local perturbations in film thickness, pressure and temperature, with the magnitude and nature of these perturbations strongly dependent on the wavelength. For the shortest wavelength ($\omega = 50$ μm), the roughness movement leads to pronounced asperity interactions, with the asperity load ratio exhibiting a sharp increase to approximately 17-18% before decreasing towards its steady state value. This is accompanied by significant fluctuations in friction and temperature with initial temperature peaks at asperity contact locations exceeding 60 °C above the baseline smooth case, indicating strong localised shear and asperity-scale heating. In contrast, for $\omega = 100$ μm and $\omega = 200$ μm, asperity interactions remain minimal, with only small transient increases in asperity load ratio below 1% and temperature peaks of about 18 and 10 °C above the baseline, respectively. Nevertheless, all cases exhibit a clear transient response as the roughness structures move through the contact, with corresponding short-term variations in friction and thermal fields.

Phase 4 ($\bar{t} \geq 25$) corresponds to a new steady state influenced by both starvation and surface topography. For the shortest wavelength ($\omega = 50$ μm), a mixed lubrication regime is established, characterised by a sustained asperity load ratio of approximately 7-10%. The coefficient of friction stabilises at approximately 0.057-0.059, exceeding both the smooth starved and fully flooded phase values, due to the significant amount of asperity contacts. The average film thickness stabilises at approximately 26-27 nm, which is higher than the smooth starved phase, suggesting local lubricant entrapment and redistribution within the contact. The average fluid temperature continues to rise even after a hydrodynamic steady state has been reached and the temperatures at the asperity locations exhibit large oscillations between approximately 30 and 55 °C above the baseline.

For the intermediate wavelength ($\omega = 100$ μm), asperity interactions remain negligible and the contact remains in a near full-film regime. The coefficient of friction decreases to values close to the fully flooded smooth phase (0.043-0.044), while the average film thickness stabilises at approximately 25 nm. This suggests that this roughness wavelength enhances lubricant entrainment and promotes film formation under starved conditions. With this wavelength, the average fluid temperature is the lowest among all cases. The temperatures at the asperity locations exhibit oscillations between approximately 0 and 17-18 °C above the baseline.

For the longest wavelength ($\omega = 200$ μm), a near full-film regime is also maintained, although with a slightly higher coefficient of friction of approximately 0.05. The average film thickness stabilises at approximately 11-12 nm. The fluid temperature continues to increase at a rate similar to that observed during the smooth starved phase, albeit with superimposed oscillations induced by the passing roughness features. Asperity temperature variations remain limited, with oscillations between approximately 0 and 10 °C above the baseline.

Further insight into the mechanisms underlying these behaviours is provided by the contour plots of oil film thickness and liquid film fraction distributions shown in Figures 14 and 15. In the smooth starved case, the outlet region is characterised by a liquid film fraction close to zero, indicating extensive cavitation. In contrast, the introduction of surface roughness leads to a noticeable increase in liquid film fraction at the outlet, with the magnitude of this effect strongly dependent on the roughness wavelength. This recovery of liquid fraction indicates that the roughness features promote local reformation of the lubricant film within regions that would otherwise remain cavitated.

For the shortest wavelength ($\omega = 50$ μm), this effect is particularly pronounced, with significant regions of non-zero liquid fraction observed throughout the outlet. This supports the earlier observation of increased average film thickness (26-27 nm), suggesting that the roughness promotes local lubricant entrapment and redistribution within the contact. However, this occurs in conjunction with strong asperity interactions, leading to increased friction and temperature values.

For the intermediate wavelength ($\omega = 100$ μm), the increase in liquid film fraction is also evident, although less pronounced. In this case, the enhanced lubricant availability contributes to the observed recovery of hydrodynamic lubrication, reflected in the reduced coefficient of friction and stabilised film thickness (approximately 25 nm). This indicates that this wavelength promotes more effective lubricant entrainment without inducing significant asperity interactions.

For the longest wavelength ($\omega = 200$ μm), the reformation of the lubricant film is the least pronounced, with only limited regions of non-zero liquid fraction observed at the outlet. This is consistent with the relatively small changes in film thickness and friction, indicating that roughness-induced lubricant redistribution becomes less effective as the wavelength increases.

The temperature distributions across the z-direction, shown in Figure 16, further highlight the strong influence of surface roughness on local thermal behaviour. For the shortest wavelength ($\omega = 50$ μm), pronounced localised hot spots are observed at asperity contact locations, extending into the adjacent solid domains. These hot spots are consistent with the elevated asperity load ratio and increased friction observed for this case and indicate intense localised heat generation due to asperity interactions.

In contrast, for the $\omega = 100$ μm and $\omega = 200$ μm cases, such localised temperature peaks are significantly less pronounced, reflecting the limited extent of asperity contact. The temperature field in these cases remains relatively smooth across the film thickness, with only minor perturbations associated with the passage of the roughness features. This behaviour is consistent with the predominantly full-film lubrication regime observed for these wavelengths.

Overall, these results demonstrate a strong dependence of the transient response on roughness wavelength. In this case, short wavelengths promote asperity interactions and localised heating, leading to increased friction and temperature, whereas intermediate wavelengths enhance lubricant entrainment and reduce both friction and temperature. Longer wavelengths exhibit an intermediate behaviour, with reduced asperity interactions but less effective film enhancement compared to the intermediate case. This highlights the complex and non-monotonic role of surface topography in starved contacts, which can now be studied extensively in one unified framework.

4.2. Case study 2

The results of case study 2 demonstrate that coating thermal properties have a pronounced influence on the thermo-mechanical response of the contact, primarily through their control of heat transport and the resulting temperature-viscosity coupling within the lubricant.

Figure 17 shows that under fully flooded conditions, clear differences are already observed between the coating configurations. The maximum fluid temperature is highest for the low TI coatings (approximately 100 °C), followed by the regular TI coatings (approximately 80 °C) and the high TI coatings (approximately 70 °C). This trend reflects the ability of the coatings to dissipate heat, with low TI coatings acting as thermal barriers, limiting heat conduction into the solids, while high TI coatings promote efficient heat removal from the contact. The COF follows the opposite trend, with values of approximately 0.013, 0.028 and 0.043 for low, regular and high TI coatings, respectively. This

behaviour is attributed to the strong temperature-viscosity coupling of the lubricant with higher fluid temperatures in the low TI case reducing the effective viscosity, thereby lowering shear stress and friction.

When starvation is imposed, these trends become more pronounced. The reduction in lubricant supply leads to thinner films and increased shear, resulting in higher temperatures across all cases. The maximum fluid temperature rises to approximately 130 °C for the system with low TI coatings, compared to approximately 90 °C for the system with regular TI coatings and a seemingly negligible rise for the system with high TI coatings. This indicates that the influence of thermal inertia becomes increasingly important under starved conditions, where heat generation is intensified and efficient heat dissipation is critical.

The evolution of the COF under starvation further highlights the interplay between thermal and hydrodynamic effects. The COF increases for all cases due to the reduction in film thickness and subsequent increase in shear stress. However, the magnitude of this increase depends strongly on the coating properties. The most significant increase is observed for the high TI coating (from approximately 0.043 to 0.063), while the regular TI case increases more moderately (from approximately 0.028 to 0.04). In contrast, the low TI coating exhibits only a small increase in COF (from approximately 0.013 to 0.019). This again reflects the importance of temperature-related reduction in viscosity, which almost offsets the increase in shear rate, hence COF, due to starvation.

The temperature distributions across the z-direction provide further insight into the role of coating thermal inertia on heat partitioning within the contact. As shown in Figures 18(a) and 19, noticeable differences are observed in the thermal gradients across the lubricant film prior to starvation. The system with high TI coatings exhibits larger temperature gradients across the film thickness, whereas the system with low TI coatings shows a more uniform temperature distribution, with the regular TI coatings system exhibiting an intermediate behaviour. Since the shear rates remain comparable across the different systems, these differences in gradients are not primarily associated with variations in viscous heat generation. Furthermore, the convective heat transport remains of similar magnitude across all cases. However, for the low TI coating, the ratio of convection through the fluid to conduction into the solids is higher, implying that a larger fraction of the generated thermal energy remains confined within the lubricant film, promoting a more uniform fluid temperature distribution across the film thickness. In contrast, the more pronounced heat conduction into the solids with high TI coatings results in steeper temperature gradients across the film thickness.

After starvation is imposed (Figures 18(c) and 20), the thermal gradients across the film are significantly reduced in all cases, resulting in a more uniform temperature distribution across the lubricant film. This is consistent with the reduction in film thickness, which causes a more uniform shear rate, thus viscous heating, across the film. As a result, temperature differences between the upper and lower surfaces diminish regardless of coating properties.

Overall, the results demonstrate that coating thermal inertia plays a critical role in controlling both temperature rise and frictional behaviour in starved contacts. Coatings with low thermal inertia lead to higher temperatures but lower friction due to viscosity reduction, whereas coatings with high thermal inertia limit fluid temperature rise but result in higher friction. The effect of starvation amplifies these differences, highlighting the importance of considering both thermal transport and transient operating conditions when evaluating coating performance.

5. Conclusions

In this work, a transient deterministic unified lubrication model was developed within a finite volume framework on a curvilinear grid. The model extends previous full-film TEHL formulations to a unified treatment of boundary, mixed and full-film lubrication regimes through the implementation of a semi-system approach. In contrast to many existing mixed lubrication studies, thermal effects within the solids are resolved directly through the solution of the energy equation, enabling the transient evolution of temperature fields within both the lubricant and solid domains to be captured without

reliance on analytical flash temperature approximations. Furthermore, the framework incorporates transient starvation, deterministic surface roughness and coating behaviour within a single unified formulation.

Two case studies were used to rigorously demonstrate the predictive capability and physical fidelity of the proposed framework. The first case study on transient starvation reveals that the system response is not continuous but organised into distinct, resolvable phases, governed by the propagation of the starvation front through the contact. Starvation induces a systematic collapse of film thickness, which in turn drives sharp increases in friction and temperature through enhanced viscous shear. Crucially, the model resolves the spatio-temporal evolution of cavitation, showing accelerated front propagation along contact edges where local pressures are lower; an effect that is typically not captured with reduced-order approaches.

Introducing deterministic roughness under starved conditions exposes a strongly non-monotonic and scale-dependent response. Short wavelength roughness ($\omega = 50$ μm) triggers persistent mixed lubrication, characterised by intense asperity interactions, elevated friction, and thermally driven hot spots extending into the solids. In contrast, intermediate wavelengths ($\omega = 100$ μm) actively promote lubricant entrainment and partial recovery of hydrodynamic lubrication, leading to counterintuitive friction reductions despite starvation. Longer wavelengths ($\omega = 200$ μm) exhibit a weaker response, with diminished redistribution effects. These results demonstrate unequivocally that surface topography is not intrinsically detrimental under starvation, but can instead be strategically tuned to enhance performance, challenging conventional design assumptions.

The second case study establishes coating thermal properties as a first-order control parameter governing coupled thermal-tribological behaviour under transient starvation. Low thermal inertia coatings lead to high lubricant temperatures due to poor heat dissipation, yet simultaneously produce lower friction via viscosity reduction. Conversely, high thermal inertia coatings suppress temperature rise but incur friction penalties due to elevated viscosity. Starvation amplifies this trade-off, highlighting that coating performance cannot be assessed under steady-state assumptions alone, and must instead be evaluated within a transient, coupled thermofluid framework.

Beyond these specific findings, the framework captures fully coupled transient heat transport across lubricant, coating, and substrate domains, resolving both through-thickness thermal gradients and the propagation of asperity-induced hot spots into the solids. This represents a clear advance over conventional flash temperature models, which cannot access such multi-domain, time-resolved behaviour.

Overall, the proposed framework establishes a step change in the modelling of transient lubrication, providing a unified, conservative, and physically grounded treatment that seamlessly bridges full-film, mixed, and boundary regimes under realistic operating conditions. By explicitly resolving the coupled dynamics of flow, roughness, starvation, and heat transport, it moves beyond descriptive analysis towards predictive, mechanism-aware simulation of tribological systems. Crucially, this capability enables the exploration of design spaces that were previously inaccessible, including the co-optimisation of surface topography and coating properties under transient, non-equilibrium conditions. Looking forward, the framework provides a natural foundation for integration with data-driven and AI-enhanced methodologies, supporting accelerated materials discovery, real-time performance prediction, and adaptive control strategies. In this context, it underpins an emerging paradigm in which tribological systems are no longer empirically tuned, but instead digitally designed, interrogated, and optimised through physics-informed virtual environments.

Appendix A. Finite Volume Discretisation

Appendix A.1. Discretisation of the Generalised Reynolds Equation

The finite volume discretisation of the dimensionless mass-conserving ($p - \theta$) generalised Reynolds equation within the semi-system lubrication framework yields the following linearised algebraic equation for each control volume:

$$\alpha(\overline{p}_W) + \beta(\overline{p}_P) + \gamma(\overline{p}_E) + \zeta(\overline{p}_N) + \lambda(\overline{p}_S) = \varphi, \tag{A1}$$

where the nodal pressures associated with the west, centre, east, north, and south neighbouring control volumes are defined as follows:

$$\overline{p}_W = \overline{p}_{i-1,j}, \qquad \overline{p}_P = \overline{p}_{i,j}, \qquad \overline{p}_E = \overline{p}_{i+1,j},$$
$$\overline{p}_N = \overline{p}_{i,j+1}, \qquad \overline{p}_S = \overline{p}_{i,j-1}.$$

The coefficients α, β, γ, ζ, and the source term φ arise from the discretisation of the diffusive, convective, and transient contributions of the governing equation. In the following expressions, the subscripts 'D', 'C', and 't' denote the diffusive, convective, and transient contributions, respectively. The lowercase directional subscripts w, e, n, and s indicate quantities evaluated at the corresponding control volume faces using arithmetic interpolation, whereby:

$$(\overline{\varepsilon})_w = \frac{(\overline{\varepsilon})_W + (\overline{\varepsilon})_P}{2}.$$

The entrainment-flow and transient terms are discretised using a second-order upwind scheme in order to improve the numerical stability and accuracy under strongly convective and transient operating conditions.

$$\begin{aligned}
\alpha_D &= \left[(\overline{\varepsilon})_w \cdot (\delta Y)_w/(\delta X)_w\right] \\
\alpha_C &= -(\delta Y)_w \cdot \Big[-2 \cdot (\overline{\rho}_e^* U_m + \overline{\rho}_1^* U_1)_{i-1} \cdot \theta_{i-1} \cdot D_{k,l}^{i,j} \\
&\quad + 0.5 \cdot (\overline{\rho}_e^* U_m + \overline{\rho}_1^* U_1)_{i-2} \cdot \theta_{i-2} \cdot D_{k-1,l}^{i-2,j}\Big] \\
\alpha_t &= -(\delta Y)_w \cdot \left[1.5 \cdot \overline{\rho}_e \cdot \theta_i \cdot D_{k-1,l}^{i,j}\right] \Big/ \Delta\bar{t} \\
\alpha &= \alpha_D + \alpha_C + \alpha_t
\end{aligned} \tag{A2}$$

$$\begin{aligned}
\beta_D &= -\left[(\overline{\varepsilon})_w \cdot (\delta Y)_w/(\delta X)_w\right] - \left[(\overline{\varepsilon})_e \cdot (\delta Y)_e/(\delta X)_e\right] \\
&\quad - r_{xy}^2\left[(\overline{\varepsilon})_n \cdot (\delta X)_n/(\delta Y)_n\right] - r_{xy}^2\left[(\overline{\varepsilon})_s \cdot (\delta X)_s/(\delta Y)_s\right] \\
\beta_C &= -(\delta Y)_w \cdot \left[1.5 \cdot (\overline{\rho}_e^* U_m + \overline{\rho}_1^* U_1)_i \cdot \theta_i \cdot D_{k,l}^{i,j} + 0.5 \cdot (\overline{\rho}_e^* U_m + \overline{\rho}_1^* U_1)_{i-2} \cdot \theta_{i-2} \cdot D_{k,l}^{i-2,j}\right] \\
\beta_t &= -(\delta Y)_w \cdot \left[1.5 \cdot \overline{\rho}_e \cdot \theta_i \cdot D_{k,l}^{i,j}\right] \Big/ \Delta\bar{t} \\
\beta &= \beta_D + \beta_C + \beta_t
\end{aligned} \tag{A3}$$

$$
\begin{aligned}
\gamma_D &= \left[(\bar{\varepsilon})_e \cdot (\delta Y)_e / (\delta X)_e\right] \\
\gamma_C &= -(\delta Y)_e \cdot \left[1.5 \cdot (\bar{\rho}_e^* U_m + \bar{\rho}_1^* U_1)_i \cdot \theta_i \cdot D_{k+1,l}^{i,j} + 0.5 \cdot (\bar{\rho}_e^* U_m + \bar{\rho}_1^* U_1)_{i-2} \cdot \theta_{i-2} \cdot D_{k+1,l}^{i-2,j}\right] \\
\gamma_t &= -(\delta Y)_e \cdot \left[1.5 \cdot \bar{\rho}_e \cdot \theta_i \cdot D_{k+1,l}^{i,j}\right] \Big/ \Delta \bar{t} \\
\gamma &= \gamma_D + \gamma_C + \gamma_t
\end{aligned}
\tag{A4}
$$

$$
\begin{aligned}
\zeta_D &= 0 \\
\zeta_C &= 0 \\
\zeta_t &= 0 \\
\zeta &= \zeta_D + \zeta_C + \zeta_t
\end{aligned}
\tag{A5}
$$

$$
\begin{aligned}
\lambda_D &= 0 \\
\lambda_C &= 0 \\
\lambda_t &= 0 \\
\lambda &= \lambda_D + \lambda_C + \lambda_t
\end{aligned}
\tag{A6}
$$

$$
\begin{aligned}
\varphi_D &= (\bar{p})_N \cdot r_{xy}^2 \left[(\bar{\varepsilon})_n \cdot (\delta X)_n / (\delta Y)_n\right] + (\bar{p})_S \cdot r_{xy}^2 \left[(\bar{\varepsilon})_s \cdot (\delta X)_s / (\delta Y)_s\right] \\
\varphi_C &= 1.5 \cdot (\bar{\rho}_e^* U_m + \bar{\rho}_1^* U_1)_i \cdot \theta_i \cdot \\
&\quad \left[H_i - \left(\left[D_{k,l}^{i,j} \cdot \bar{p}_{k,l}\right] + \left[D_{k+1,l}^{i,j} \cdot \bar{p}_{k+1,l}\right]\right)\right] \\
&\quad - 2 \cdot (\bar{\rho}_e^* U_m + \bar{\rho}_1^* U_1)_{i-1} \cdot \theta_{i-1} \cdot \\
&\quad \left[H_{i-1} - \left[D_{k-1,l}^{i-1,j} \cdot \bar{p}_{k-1,l}\right]\right] \\
&\quad + 0.5 \cdot (\bar{\rho}_e^* U_m + \bar{\rho}_1^* U_1)_{i-2} \cdot \theta_{i-2} \cdot \\
&\quad \left[H_{i-2} - \left(\left[D_{k-1,l}^{i-2,j} \cdot \bar{p}_{k-2,l}\right] + \left[D_{k,l}^{i-2,j} \cdot \bar{p}_{k,l}\right] + \left[D_{k+1,l}^{i-2,j} \cdot \bar{p}_{k+1,l}\right]\right)\right] \\
\varphi_t &= \left\{1.5 \cdot \bar{\rho}_e \cdot \theta_i \cdot \left[H_i - \left(\left[D_{k-1,l}^{i,j} \cdot \bar{p}_{k-1,l}\right] + \left[D_{k,l}^{i,j} \cdot \bar{p}_{k,l}\right] + \left[D_{k+1,l}^{i,j} \cdot \bar{p}_{k+1,l}\right]\right)\right]\right. \\
&\quad - 2 \cdot \bar{\rho}_e^{N-1} \cdot \theta_i^{N-1} \cdot H_i^{N-1} \\
&\quad \left. + 0.5 \cdot \bar{\rho}_e^{N-2} \cdot \theta_i^{N-2} \cdot H_i^{N-2}\right\} \Big/ \Delta \bar{t} \\
\varphi &= \varphi_D + \varphi_C + \varphi_t
\end{aligned}
\tag{A7}
$$

Table A1. Normalised variables and discretisation parameters used in the finite volume formulation of the semi-system generalised Reynolds equation.

Symbol	Parameter	Definition
$D_{k,l}^{i,j}$	Influence coefficient relating the pressure at node (k,l) to the elastic deformation at node (i,j)	–
H	Normalised film thickness	h/a
$\overline{p}$	Normalised pressure	p/p_{Hertz}
N	Time level	–
r_{xy}	Grid aspect ratio	$\Delta x/\Delta y$
U_1, U_2	Normalised velocities of the lower and upper surfaces in the sliding direction	u_1/u_{ent}, u_2/u_{ent}
U_m	Normalised mean entrainment velocity	$(U_1+U_2)/2$
$\Delta\overline{t}$	Normalised time step	$\Delta t\, u_{\text{ent}}/a$
$\delta X, \delta Y$	Normalised control volume face dimensions in the x- and y-directions	$\delta x/a$, $\delta y/a$
$(\delta X)_{w,e}$	Normalised distances between neighbouring nodes in the west and east directions	–
$(\delta Y)_{n,s}$	Normalised distances between neighbouring nodes in the north and south directions	–
$(\delta Y)_{w,e}$, $(\delta X)_{n,s}$	Normalised face lengths associated with west/east and north/south control volume faces	–
$\overline{\varepsilon}$	Normalised pressure-flow coefficient in the generalised Reynolds equation	$\varepsilon\,\eta_0/(\rho_0 a^3)$
$\overline{\rho}_e$	Normalised equivalent density integrated across the film thickness	$\rho_e/(\rho_0 a)$
$\overline{\rho}_e^*$	Normalised entrainment-flow density coefficient	ρ_e^*/ρ_0
$\overline{\rho}_1^*$	Normalised surface-velocity density coefficient	ρ_1^*/ρ_0
θ	Lubricant film fraction	$0 \le \theta \le 1$
$\alpha, \beta, \gamma, \zeta, \lambda$	Algebraic coefficients associated with west, central, east, north, and south pressure nodes	–
φ	Source term of the discretised Reynolds equation	–

Appendix A.2. Discretisation of the Fluid Energy Equation

The dimensionless energy equation governing thermal transport within the lubricant film is presented below for a general non-orthogonal curvilinear coordinate system, following the formulation proposed by Ardah et al. [27]:

$$\mathrm{Pe}\left[\frac{\partial(H\overline{\rho c}\,\overline{T})}{\partial\overline{t}}\right] + \mathrm{Pe}\left[\boldsymbol{\nabla}_{\boldsymbol{X}}\cdot(\overline{\rho c}\tilde{\boldsymbol{V}}\overline{T})\right] = \boldsymbol{\nabla}_{\boldsymbol{X}}\cdot\left(\left[\tilde{\overline{\kappa}}\right]\boldsymbol{\nabla}_{\boldsymbol{X}}\overline{T}\right) + \overline{\tilde{Q}}_p + \overline{\tilde{Q}}_c + \overline{\tilde{Q}}_\Phi + \overline{\tilde{\dot{q}}}_V. \tag{A8}$$

The dimensionless variables and source terms are defined as follows:

$$H = \frac{h}{a}, \quad \overline{\rho} = \frac{\rho}{\rho_0}, \qquad \overline{c} = \frac{c}{c_0},$$

$$\overline{T} = \frac{T}{T_0}, \quad \overline{\eta} = \frac{\eta}{\eta_0}, \qquad \overline{\beta} = \frac{\beta}{\beta_0},$$

$$\epsilon = \frac{h_c}{a}, \quad \overline{p} = \frac{p\epsilon^2 a}{\eta_0 u_{ent}}.$$

The normalised source-term contributions associated with compressive heating/cooling ($\overline{\tilde{Q}}_p$), enthalpic effects ($\overline{\tilde{Q}}_c$), viscous dissipation ($\overline{\tilde{Q}}_\Phi$), and volumetric heat generation ($\overline{\tilde{\dot{q}}}_V$) are expressed as follows

$$\overline{\tilde{Q}}_p = \mathrm{Br}^*\overline{\beta T}\left(H\frac{\partial\overline{p}}{\partial\overline{t}} + \tilde{V}^X\frac{\partial\overline{p}}{\partial X} + \tilde{V}^Y\frac{\partial\overline{p}}{\partial Y}\right),$$

$$\overline{\tilde{Q}}_c = \mathrm{Pe}\overline{\rho}\,\overline{T}\left(H\frac{\partial \overline{c}}{\partial \overline{t}} + \tilde{\boldsymbol{V}}\cdot\boldsymbol{\nabla}_X\overline{c}\right),$$

$$\overline{\tilde{Q}}_\Phi = \frac{\mathrm{Br}\,\overline{\eta}}{H^3}\left[\left(\frac{\partial \tilde{V}^X}{\partial Z}\right)^2 + \left(\frac{1}{r_{xy}}\frac{\partial \tilde{V}^Y}{\partial Z}\right)^2\right],$$

$$\overline{\tilde{\tilde{q}}}_V = H\tilde{\tilde{q}}_V.$$

The governing dimensionless groups appearing in the thermal formulation are given as follows:

$$\mathrm{Pe} = \frac{\rho_0 c_0 u_{ent} a\epsilon^2}{k_0}, \qquad \mathrm{Br} = \frac{\eta_0 u_{ent}^2}{k_0 T_0}, \qquad \mathrm{Br}^* = \beta_0 T_0 \mathrm{Br},$$

where Pe is the Peclet number, Br is the Brinkman number, and Br^* is the modified Brinkman number.

The finite volume discretisation of the dimensionless energy equation is obtained by combining the spatial discretisation procedure proposed by Ardah et al. [27] with a first-order backward temporal discretisation following the approach outlined by in [50]. The resulting discretised formulation is presented below.

$$\begin{aligned}\mathrm{Pe}\,(\Delta V_{CV})_P\frac{\left(H\overline{\rho}\,\overline{c}\,\overline{T}_P\right)^N - \left(H\overline{\rho}\,\overline{c}\,\overline{T}_P\right)^{N-1}}{\Delta\overline{t}} \\ + \alpha\overline{T}_W + \beta\overline{T}_P + \gamma\overline{T}_E + \zeta\overline{T}_N + \lambda\overline{T}_S + \phi\overline{T}_T + \psi\overline{T}_B = \varphi.\end{aligned} \tag{A9}$$

The neighbouring temperature values appearing in Equation A9 correspond to west, central, east, north, south, top, and bottom nodes of the control volume and are defined as follows:

$$\begin{aligned}&\overline{T}_W = \overline{T}_{i-1,j,k}, \quad \overline{T}_P = \overline{T}_{i,j,k}, \quad \overline{T}_E = \overline{T}_{i+1,j,k},\\ &\overline{T}_N = \overline{T}_{i,j+1,k}, \quad \overline{T}_S = \overline{T}_{i,j-1,k}, \quad \overline{T}_T = \overline{T}_{i,j,k+1},\\ &\overline{T}_B = \overline{T}_{i,j,k-1}.\end{aligned}$$

The coefficients α, β, γ, ζ, λ, ϕ, ψ and φ are defined below. In these expression, the subscripts 'D' and 'C' refer to the the diffusive and convective contributions arising from the diffusive and convective terms of the energy equation, respectively.

$$\begin{aligned}\alpha_D &= -(\epsilon)^2\cdot\overline{k}_w\cdot H_w\cdot S_w/(\delta X)_w\\ \alpha_C &= -\left[\left[\left(\overline{\rho c}\tilde{V}^X\right)_w\cdot\mathrm{Pe}\cdot S_w,\ 0\right]\right]\\ \alpha &= \alpha_D + \alpha_C\end{aligned} \tag{A10}$$

$$\begin{aligned}\gamma_D &= -(\epsilon)^2\cdot\overline{k}_e\cdot H_e\cdot S_e/(\delta X)_e\\ \gamma_C &= -\left[\left[-\left(\overline{\rho c}\tilde{V}^X\right)_e\cdot\mathrm{Pe}\cdot S_e,\ 0\right]\right]\\ \gamma &= \gamma_D + \gamma_C\end{aligned} \tag{A11}$$

$$\begin{aligned}\zeta_D &= -(r_{xy}\epsilon)^2\cdot\overline{k}_n\cdot H_n\cdot S_n/(\delta Y)_n\\ \zeta_C &= -\left[\left[-\left(\overline{\rho c}\tilde{V}^Y\right)_n\cdot\mathrm{Pe}\cdot S_n,\ 0\right]\right]\\ \zeta &= \zeta_D + \zeta_C\end{aligned} \tag{A12}$$

$$\begin{aligned}\lambda_D &= -(r_{xy}\epsilon)^2\cdot\overline{k}_s\cdot H_s\cdot S_s/(\delta Y)_s\\ \lambda_C &= -\left[\left[\left(\overline{\rho c}\tilde{V}^Y\right)_s\cdot\mathrm{Pe}\cdot S_s,\ 0\right]\right]\\ \lambda &= \lambda_D + \lambda_C\end{aligned} \tag{A13}$$

$$
\begin{aligned}
\phi_D &= -(\bar{k}_t \cdot S_t) \cdot \left[1 + \left(\epsilon^2 \cdot \left[\left(\nabla_X \cdot H\right)_t\right]^2 \cdot Z_t^2\right)\right. \\
&\quad \left. + \left(\left(\epsilon r_{xy}\right)^2 \cdot \left[\left(\nabla_Y \cdot H\right)_t\right]^2\right) \cdot Z_t^2\right] / \left(H \cdot (\delta Z)_t\right) \\
\phi_C &= -\left[\left[-\left(\overline{\rho c}\tilde{V}^Z\right)_t \cdot \mathrm{Pe} \cdot S_t,\ 0\right]\right] \\
\phi &= \phi_D + \phi_C
\end{aligned}
\tag{A14}
$$

$$
\begin{aligned}
\psi_D &= -(\bar{k}_b \cdot S_b) \cdot \left[1 + \left(\epsilon^2 \cdot \left[\left(\nabla_X \cdot H\right)_b\right]^2 \cdot Z_b^2\right)\right. \\
&\quad \left. + \left(\left(\epsilon r_{xy}\right)^2 \cdot \left[\left(\nabla_Y \cdot H\right)_b\right]^2\right) \cdot Z_b^2\right] / \left(H \cdot (\delta Z)_b\right) \\
\psi_C &= -\left[\left[\left(\overline{\rho c}\tilde{V}^Z\right)_b \cdot \mathrm{Pe} \cdot S_b,\ 0\right]\right] \\
\psi &= \psi_D + \psi_C
\end{aligned}
\tag{A15}
$$

$$
\begin{aligned}
\beta_D &= -\alpha_D - \gamma_D - \zeta_D - \lambda_D - \phi_D - \psi_D \\
\beta_C &= \left[\left[\left(\overline{\rho c}\tilde{V}^X\right)_e \cdot \mathrm{Pe} \cdot S_e,\ 0\right]\right] \\
&\quad + \left[\left[\left(\overline{\rho c}\tilde{V}^Y\right)_n \cdot \mathrm{Pe} \cdot S_n,\ 0\right]\right] \\
&\quad + \left[\left[\left(\overline{\rho c}\tilde{V}^Z\right)_t \cdot \mathrm{Pe} \cdot S_t,\ 0\right]\right] \\
&\quad + \left[\left[-\left(\overline{\rho c}\tilde{V}^X\right)_w \cdot \mathrm{Pe} \cdot S_w,\ 0\right]\right] \\
&\quad + \left[\left[-\left(\overline{\rho c}\tilde{V}^Y\right)_s \cdot \mathrm{Pe} \cdot S_s,\ 0\right]\right] \\
&\quad + \left[\left[-\left(\overline{\rho c}\tilde{V}^Z\right)_b \cdot \mathrm{Pe} \cdot S_b,\ 0\right]\right] \\
\beta &= \beta_D + \beta_C
\end{aligned}
\tag{A16}
$$

$$
\varphi = \left[\left(\overline{\tilde{Q}}_p\right)_P + \left(\overline{\tilde{Q}}_c\right)_P + \left(\overline{\tilde{Q}}_\Phi\right)_P + \left(\bar{\tilde{q}}_V\right)_P\right] \cdot (\Delta V_{CV})_P \tag{A17}
$$

The operator $\left[\left[A, B\right]\right]$ denotes the maximum between A and B. The lowercase subscripts w, e, n, s, t, and b indicate the quantities evaluated at the corresponding control volume faces using arithmetic averaging. For example,

$$
(\bar{c})_w = \frac{(\bar{c})_W + (\bar{c})_P}{2}.
$$

Table A2. Normalised variables and discretisation parameters used in the finite volume formulation of the lubricant energy equation.

Symbol	Parameter	Definition
$\overline{c}$	Normalised specific heat capacity	c/c_0
H	Normalised lubricant film thickness	h/a
$[\overline{\tilde{\boldsymbol{\kappa}}}]$	Dimensionless diffusion tensor in the transformed coordinate system	–
$\overline{p}$	Normalised pressure	$p\epsilon^2 a/(\eta_0 u_{\text{ent}})$
$\boldsymbol{S}$	Outward surface vector normal to a control-volume face	–
$\overline{T}$	Normalised temperature	T/T_0
$\tilde{\boldsymbol{V}}$	Dimensionless contravariant velocity vector in the transformed domain	$\left[\tilde{V}^X, \tilde{V}^Y, \tilde{V}^Z\right]^T$
$\tilde{V}^X, \tilde{V}^Y, \tilde{V}^Z$	Dimensionless contravariant velocity components in the X-, Y-, and Z-directions	–
X, Y, Z	Normalised coordinates in the sliding, transverse, and film-thickness directions	$x/a, y/a, z/h$
$\overline{\beta}$	Normalised coefficient of thermal expansion	β/β_0
$\delta X, \delta Y, \delta Z$	Normalised control-volume dimensions in the transformed coordinate directions	–
ΔV_{CV}	Control-volume volume in the transformed domain	$(\delta X)(\delta Y)(\delta Z)$
ϵ	Film-thickness-to-contact-length scale ratio	h_c/a
$\overline{\eta}$	Normalised dynamic viscosity	η/η_0
$\overline{\rho}$	Normalised density	ρ/ρ_0
Pe	Peclet number	$\rho_0 c_0 u_{\text{ent}} a\epsilon^2/k_0$
Br	Brinkman number	$\eta_0 u_{\text{ent}}^2/(k_0 T_0)$
Br*	Modified Brinkman number	$\beta_0 T_0 \text{Br}$

Appendix A.3. Discretisation of Heat Transport in Solid and Coated Domains

The finite volume discretisation of the energy equation within the coating and substrate domains follows the same procedure as that used for the lubricant energy equation presented in Section A.2. The principal distinction is that no volumetric heat-generation source terms are included within the solid regions, since heat generation is assumed to arise predominantly from viscous dissipation within the lubricant film and frictional heating at asperity contact locations. Consequently, thermal transport in the solid domains is governed primarily by transient heat conduction and convective transport associated with the motion of the bounding surfaces. The in-plane discretisation in the x- and y-directions remains fully consistent with that employed for the lubricant domain, thereby preserving spatial compatibility across the coupled fluid-solid system. In contrast, the out-of-plane discretisation in the z-direction is defined according to the physical thickness of each coating layer and substrate region. This enables the thermal response of thin coatings, multilayered interfaces, and bulk substrates to be resolved accurately within the coupled thermo-hydrodynamic formulation.

To accurately capture the thermal gradients that develop near the interfaces, local mesh refinement is introduced in the vicinity of the fluid-coating and coating-substrate interfaces. In particular, increased mesh resolution in the z-direction ensures accurate evaluation of the interfacial heat fluxes and temperature gradients governing thermal continuity across neighbouring domains.The thermal coupling between neighbouring domains is enforced through the heat-flux continuity conditions given by Equation 19 and Equation 20. Equation 19 ensures continuity of conductive heat flux across fluid-solid interfaces, while Equation 20 governs heat transfer across asperity contact regions by accounting for frictionally generated heat at solid-solid junctions, hence ensuring thermodynamic consistency throughout the coupled conjugate heat-transfer problem.

References

1. Lugt, P.M.; Morales-Espejel, G.E. A review of elasto-hydrodynamic lubrication theory. *Tribology Transactions* **2011**, *54*, 470–496. https://doi.org/10.1080/10402004.2010.551804.

2. Ardah, S.; Profito, F.J.; Dini, D. A comprehensive review and trends in lubrication modelling. *Advances in Colloid and Interface Science* **2025**, *342*, 103492. https://doi.org/10.1016/j.cis.2025.103492.
3. Morales-Espejel, G.E.; Wemekamp, A.W. Ertel-Grubin method in elastohydrodynamic lubrication - A review. *Proceedings of the Institution of Mechanical Engineers, Part J* **2008**, *222*, 15–34. https://doi.org/10.1243/13506501JET325.
4. Cann, P.M.E.; Damiens, B.; Lubrecht, A.A. The transition between fully flooded and starved regimes in EHL. *Tribology International* **2004**, *37*, 859–864. https://doi.org/10.1016/j.triboint.2004.05.005.
5. Bijani, D.; Deladi, E.L.; de Rooij, M.B.; Schipper, D.J. The influence of surface texturing on the frictional behaviour in starved lubricated parallel sliding contacts. *Lubricants* **2019**, *7*, 68. https://doi.org/10.3390/lubricants7080068.
6. Wang, X.; Liu, Y.; Zhu, D. Numerical Solution of Mixed Thermal Elastohydrodynamic Lubrication in Point Contacts With Three-Dimensional Surface Roughness. *Journal of Tribology* **2017**, *139*. https://doi.org/10.1115/1.4032963.
7. Decote, M.; Fillot, N.; Mahéo, Y.; Morales-Espejel, G.E. An Original Methodology to Model Stationary and Transient Starvation in Elastohydrodynamic Lubrication Contact. *Journal of Tribology* **2024**, *146*. https://doi.org/10.1115/1.4064398.
8. Morales-Espejel, G.E. Surface roughness effects in elastohydrodynamic lubrication: A review with contributions. *Proceedings of the Institution of Mechanical Engineers, Part J* **2014**, *228*, 1217–1242. https://doi.org/10.1177/1350650113513572.
9. Wang, W.Z.; Li, S.; Shen, D.; Zhang, S.; Hu, Y. A mixed lubrication model with consideration of starvation and interasperity cavitations. *Proceedings of the Institution of Mechanical Engineers, Part J: Journal of Engineering Tribology* **2012**, *226*. https://doi.org/10.1177/1350650112460830.
10. Ebner, M.; Yilmaz, M.; Lohner, T.; Michaelis, K.; Höhn, B.R.; Stahl, K. On the effect of starved lubrication on elastohydrodynamic (EHL) line contacts. *Tribology International* **2018**, *118*. https://doi.org/10.1016/j.triboint.2017.06.004.
11. Yin, C.; Yang, P.; Tan, H.; Wang, J. Thermal elastohydrodynamic lubrication of starved elliptical contacts. *Tribology International* **2009**, *42*. https://doi.org/10.1016/j.triboint.2009.01.007.
12. Liu, M.; Ku, H.; Zhang, J.; Xu, P.; Wu, C. Predicting Fatigue Life for Finite Line Contact under Starved Elastohydrodynamic Lubrication Condition. *Mathematical Problems in Engineering* **2020**, *2020*. https://doi.org/10.1155/2020/5928621.
13. Wen, C.; Meng, X.; Gu, J.; Xiao, L.; Jiang, S.; Bi, H. Starved lubrication analysis of angular contact ball bearing based on a multi-degree-of-freedom tribo-dynamic model. *Friction* **2023**, *11*. https://doi.org/10.1007/s40544-022-0661-2.
14. Pu, W.; Zhu, D.; Wang, J. A Starved Mixed Elastohydrodynamic Lubrication Model for the Prediction of Lubrication Performance, Friction and Flash Temperature with Arbitrary Entrainment Angle. *Journal of Tribology* **2018**, *140*. https://doi.org/10.1115/1.4037844.
15. Carslaw, H.S.; Jaeger, J.C. Some Two-Dimensional Problems in Conduction of Heat with Circular Symmetry. *Proceedings of the London Mathematical Society* **1940**, *s2-46*, 361–388. https://doi.org/10.1112/plms/s2-46.1.361.
16. Zhu, D.; Wang, J.; Wang, Q.J. On the Stribeck Curves for Lubricated Counterformal Contacts of Rough Surfaces. *Journal of Tribology* **2015**, *137*. https://doi.org/10.1115/1.4028881.
17. Archard, J. The temperature of rubbing surfaces. *Wear* **1959**, *2*, 438–455. https://doi.org/10.1016/0043-1648(59)90159-0.
18. Liu, Y.; Chen, W.W.; Zhu, D.; Liu, S.; Wang, Q.J. An elastohydrodynamic lubrication model for coated surfaces in point contacts. *Journal of Tribology* **2007**, *129*, 509–516. https://doi.org/10.1115/1.2736433.
19. Habchi, W. A numerical model for the solution of thermal elastohydrodynamic lubrication in coated circular contacts. *Tribology International* **2014**, *73*, 57–68. https://doi.org/10.1016/j.triboint.2014.01.002.
20. Ai, X. Numerical Analyses of Elastohydrodynamically Lubricated Line and Point Contacts with Rough Surfaces By Using Semi-system and Multigrid Methods. PhD thesis, Northwestern University, 1993.
21. Hajishafiee, A.; Dini, D.; Kadiric, A.; Ioannides, S. A fully-coupled finite volume CFD solver for elastohydrodynamic lubrication problems with particular application to rolling element bearings. *Tribology International* **2017**, *109*, 258–273. https://doi.org/10.1016/j.triboint.2016.12.046.
22. Singh, K.; Sadeghi, F.; Russell, T.; Lorenz, S.J.; Peterson, W.; Villarreal, J.; Jinmon, T. Fluid-Structure Interaction Modeling of Elastohydrodynamically Lubricated Line Contacts. *Journal of Tribology* **2021**, *143*, 091602. https://doi.org/10.1115/1.4049260.

23. Layton, J.; Rothwell, B.C.; Ambrose, S.; Eastwick, C.; Medina, H.; Rebelo, N. A New Thermal Elasto-Hydrodynamic Lubrication Solver Implementation in OpenFOAM. *Lubricants* **2023**, *11*, 308. https://doi.org/10.3390/lubricants11070308.
24. Hansen, E.; Kacan, A.; Frohnapfel, B.; Codrignani, A. An EHL Extension of the Unsteady FBNS Algorithm. *Tribology Letters* **2022**, *70*, 80. https://doi.org/10.1007/s11249-022-01615-1.
25. Ardah, S.; Profito, F.J.; Dini, D. Modelling heterogeneous interfaces using element-based finite volumes. *Computer Methods in Applied Mechanics and Engineering* **2026**, *458*, 118986. https://doi.org/10.1016/j.cma.2026.118986.
26. Ardah, S.; Profito, F.J.; Dini, D. An integrated finite volume framework for thermal elasto-hydrodynamic lubrication. *Tribology International* **2023**, *177*, 107935. https://doi.org/10.1016/j.triboint.2022.107935.
27. Ardah, S.; Profito, F.J.; Reddyhoff, T.; Dini, D. Advanced modelling of lubricated interfaces in general curvilinear grids. *Tribology International* **2023**, *188*, 108727. https://doi.org/10.1016/j.triboint.2023.108727.
28. Kaliafetis, F.; Ardah, S.; Ewen, J.P.; Dini, D. Using artificial neural networks to accelerate thermo-elastohydrodynamic lubrication simulations. *Tribology International* **2025**, *212*. https://doi.org/10.1016/j.triboint.2025.110978.
29. Wang, Q.; Zhu, D. *Interfacial Mechanics*; CRC Press, 2019. https://doi.org/10.1201/9780429131011.
30. Dowson, D. A generalized Reynolds equation for fluid-film lubrication. *International Journal of Mechanical Sciences* **1962**, *4*, 159–170. https://doi.org/10.1016/S0020-7403(62)80038-1.
31. Elrod, H.G.; Adams, M.L. A computer program for cavitation and starvation problems. In Proceedings of the Cavitation and related phenomena in lubrication: proceedings of the 1st Leeds-Lyon Symposium on Tribology. Department of Mechanical Engineering, The University of Leeds, England, 1974, pp. 37–41.
32. Elrod, H.G. A general theory for laminar lubrication with Reynolds roughness. *Journal of Lubrication Technology* **1979**, *101*, 8–14. https://doi.org/10.1115/1.3453283.
33. Elrod, H.G. A cavitation algorithm. *Journal of Lubrication Technology* **1981**, *103*, 350–354. https://doi.org/10.1115/1.3251669.
34. Jakobsson, B. The Finite Journal Bearing Considering Vaporization. *Trans. Chalmers Univ. of Tech, Sweden* **1965**, *190*.
35. Floberg, L. On hydrodynamic lubrication with special reference to sub-cavity pressures and number of streamers in cavitation regions. *Acta Polytechnica Scandinavica* **1965**, *Mechanical Engineering Series 19*.
36. Floberg, L. *On the Tensile Strength of Liquids*; Transactions of Machine Elements Division / Lund Technical University, Lund, Sweden, Lund Technical University, 1973.
37. Hu, Y.; Zhu, D. A Full Numerical Solution to the Mixed Lubrication in Point Contacts. *Journal of Tribology* **2000**, *122*, 1–9. https://doi.org/10.1115/1.555322.
38. Liu, S.; Wang, Q.; Liu, G. A versatile method of discrete convolution and FFT (DC-FFT) for contact analyses. *Wear* **2000**, *243*, 101–111. https://doi.org/10.1016/S0043-1648(00)00427-0.
39. Wang, Q.J.; Sun, L.; Zhang, X.; Liu, S.; Zhu, D. FFT-Based Methods for Computational Contact Mechanics. *Frontiers in Mechanical Engineering* **2020**, *6*. https://doi.org/10.3389/fmech.2020.00061.
40. Yu, C.; Wang, Z.; Wang, Q. Analytical frequency response functions for contact of multilayered materials. *Mechanics of Materials* **2014**, *76*, 102–120. https://doi.org/10.1016/j.mechmat.2014.06.006.
41. Wang, Z.; Yu, C.; Wang, Q. Model for Elastohydrodynamic Lubrication of Multilayered Materials. *Journal of Tribology* **2015**, *137*. https://doi.org/10.1115/1.4028408.
42. Roelands, C.J.A.; Winer, W.O.; Wright, W.A. Correlational Aspects of the Viscosity-Temperature-Pressure Relationship of Lubricating Oils (Dr In dissertation at Technical University of Delft, 1966). *Journal of Lubrication Technology* **1971**, *93*, 209–210. https://doi.org/10.1115/1.3451519.
43. Eyring, H. Viscosity, Plasticity, and Diffusion as Examples of Absolute Reaction Rates. *The Journal of Chemical Physics* **1936**, *4*, 283–291. https://doi.org/10.1063/1.1749836.
44. Dowson, D.; Higginson, G.R. A Numerical Solution to the Elasto-Hydrodynamic Problem. *Journal of Mechanical Engineering Science* **1959**, *1*, 6–15. https://doi.org/10.1243/jmes_jour_1959_001_004_02.
45. Dowson, D.; Higginson, G. *Elasto-Hydrodynamic Lubrication*, 1st ed.; Vol. 23, Pergamon Press, 1977. https://doi.org/10.1016/C2013-0-05764-7.
46. Venner, C.H.; Lubrecht, A.A. Numerical Simulation of a Transverse Ridge in a Circular EHL Contact Under Rolling/Sliding. *Journal of Tribology* **1994**, *116*, 751–761. https://doi.org/10.1115/1.2927329.
47. Venner, C.H.; Lubrecht, A.A. Multilevel methods in lubrication. *Tribology Series* **2000**, *37*. https://doi.org/10.1243/1350650011543727.

48. Ai, X.; Cheng, H.S. The Influence of Moving Dent on Point EHL Contacts. *Tribology Transactions* **1994**, *37*, 323–335. https://doi.org/10.1080/10402009408983301.
49. Cui, J.; Yang, P.; Kaneta, M.; Krupka, I. Numerical study on the interaction of transversely oriented ridges in thermal elastohydrodynamic lubrication point contacts using the Eyring shear-thinning model. *Proceedings of the Institution of Mechanical Engineers, Part J: Journal of Engineering Tribology* **2017**, *231*, 93–106. https://doi.org/10.1177/1350650116646943.
50. Moukalled, F.; Mangani, L.; Darwish, M. *The Finite Volume Method in Computational Fluid Dynamics*; Vol. 113, Springer International Publishing, 2016. https://doi.org/10.1007/978-3-319-16874-6.